Convective Circulations and the Coriolis Force: A Mechanism for Upscale Momentum Fluxes in the Tropics

EDWARD J. GOLDSMITH,[a] JOSEPH A. BIELLO,[a] AND MATTHEW R. IGEL[b]

[a] *Department of Mathematics, University of California, Davis, Davis, California*
[b] *Department of Land, Air and Water Resources, University of California, Davis, Davis, California*

(Manuscript received 18 August 2024, in final form 10 January 2025, accepted 31 January 2025)

ABSTRACT: In the study of subgrid-scale tropical convection, the importance of retaining the frequently omitted "nontraditional" component of the Coriolis force is increasingly being recognized. A number of recent papers have developed linear theories examining the behavior of a diabatic heat-source-driven convective circulation in the presence of the full Coriolis force, and it was shown that the nontraditional Coriolis terms drive vertical shears on the large scales through upscale fluxes of momentum. In the present work, we generalize these results to the nonlinear regime, using a formal asymptotic theory based upon the fact that rotation is a second-order effect compared with advection by the vertical component of velocity at subgrid scales. Ultimately, we demonstrate that the same basic flow structures persist, with a particular emphasis on the counterrotating vortex pair induced by the nontraditional Coriolis terms which drive a westward tilt in convection. We compute the form of the upscale momentum flux convergence in the nonlinear regime, greatly extending the regimes of validity provided by the simple analytical expressions previously given in the linear case. This study constitutes an important step toward being able to accurately and consistently parameterize the large-scale vertical shear driven by nonlinear, subgrid convective processes under the influence of the nontraditional Coriolis force terms.

KEYWORDS: Tropics; Cloud forcing; Convective clouds; Fluxes; Nonlinear dynamics; Convective parameterization

1. Introduction

Upon reading any introductory meteorological textbook, one will quickly be confronted with the *Coriolis force* which acts upon objects contained within a rotating reference frame (Coriolis 1835; Poisson 1838). Indeed, Earth's rotation may be considered the fundamental mechanism which solidifies the theory of atmospheric and oceanic fluid dynamics as distinct subjects from other fluid dynamical theories, and thus, it is difficult to overexaggerate its importance as a physical constraint.

Using the *f*-plane approximation, the Coriolis force, as it appears in the primitive momentum equations, is given by

$$\mathbf{F}^C = -2\Omega \sin\lambda \hat{\mathbf{z}} \times \mathbf{v} - 2\Omega \cos\lambda \hat{\mathbf{y}} \times \mathbf{v}, \tag{1}$$

where $\mathbf{v}$ is the velocity field, Ω is the rotation rate of Earth, and λ is the latitude. In the context of nonlinear convective processes, studies involving phenomena, such as cyclogenesis and hurricane formation (e.g., Charney and Eliassen 1964; Smith 1980; Rotunno and Emanuel 1987; Montgomery and Farrell 1993), mesoscale convective circulations (e.g., Held and Hou 1980; Emanuel et al. 1994), and buoyant jets (e.g., Deremble 2016; Sutherland et al. 2021) to name just a few, have focused primarily on the *traditional Coriolis terms* (TCTs)—i.e., those terms in Eq. (1) proportional to the sine of latitude. However, in the literature, comparatively little attention has been given to the remaining terms, i.e., those proportional to the cosine of latitude, which have come to be known as the *nontraditional Coriolis terms* (NCTs). Holton (2004) justifies the traditional Coriolis approximation by noting that on synoptic scales, the vertical component of velocity is vanishingly small compared with the horizontal components, and that on smaller scales, rotation rarely enters the dynamics at leading order. Liang and Chan (2005), however, recognized that in localized weather patterns where vertical and horizontal motions may appear at the same order, the traditional approximation is no longer appropriate, especially in the tropics where $\sin\lambda \ll \cos\lambda$. The purpose of our study is to investigate the effects of rotation on a steady nonlinear convective circulation driven by an axisymmetric heat source, where we retain both the TCT and NCT components of the Coriolis force. Although we are primarily motivated by the potential application of these results in cloud models, we do not consider thermodynamic effects here, and thus we are not truly modeling "clouds" at this stage.

There are two main bodies of work which our study aims to connect with and generalize. The first of these involves the linear theory of convective circulations under the influence of the full Coriolis force developed by Marsico et al. (2023, 2024) in conjunction with the dynamics of nonrotating updraft torii (DoNUT) convective parameterization framework proposed by Igel and Biello (2020). These studies show that within an appropriate scaling regime whereby rotation, damping, and the pressure gradient all exist in a leading order balance, analytical solutions to the convective circulation problem are possible. These solutions are shown to be comprised of two distinct components—the primary *poloidal* component of the flow, whereby the vertical velocity is prescribed by the form of the heating through a diagnostic relationship (the *weak temperature gradient* approximation), and a secondary component of the flow induced by rotation, which exists entirely

Corresponding author: Edward J. Goldsmith, ejgoldsmith@ucdavis.edu

DOI: 10.1175/JAS-D-24-0160.1

© 2025 American Meteorological Society. This published article is licensed under the terms of the default AMS reuse license. For information regarding reuse of this content and general copyright information, consult the AMS Copyright Policy (www.ametsoc.org/PUBSReuseLicenses).

Brought to you by UNIVERSITY OF CALIFORNIA Davis - SERIALS RECORDS SECTION | Unauthenticated | Downloaded 07/14/25 03:45 PM UTC

within the horizontal plane. For a prescribed sinusoidal heating, the rotation induced component of the flow contains contributions from both the TCT and NCT, with the TCT driving lower-level cyclonic and upper-level anticyclonic rotation and the NCT accelerating upward moving air toward the west, driving a westward-pointing, midlevel dipole. Our study proceeds based upon a different scaling where nonlinear effects are retained, and the Coriolis terms provide corrections at an asymptotically higher order. While Marsico et al. (2023, 2024) is able to separate out the flow components utilizing the Helmholtz decomposition (Helmholtz 1867; Lebovitz 1989), our analysis proceeds using an asymptotic expansion, whereby the poloidal flow is found at leading order, and the induced flow is found as a solution to a linear PDE at order Ro^{-1}, where $\mathrm{Ro} \gg 1$ is the Rossby number. Most notably, the same basic flow structure is preserved in the nonlinear case as well as throughout a number of different damping regimes, demonstrating that Marsico's result is not merely a fluke of linearity.

The second key body of work has its origins in the seminal paper of LeMone (1983), who derived momentum fluxes from a system of equations which include both the TCT and NCT. In measured fluxes from a mesoscale convective system observed during the GARP Atlantic Tropical Experiment, she noted that the contributions of the NCT to vertical fluxes of zonal momentum are not only important within a storm but also the leading-order contribution outside of storms. Recently, Biello et al. (2024, manuscript submitted to *Quart. J. Roy. Meteor. Soc.*) have developed a more general understanding of the importance of the NCT on the vertical flux of horizontal momentum in convective circulations. Beyond inspiring results from LeMone, their motivation has been a simple logic. The NCT couples the zonal and vertical momentum equations, while convective circulations likewise represent a marriage of horizontal and vertical flows. Much like LeMone (1983), Biello et al. (2024, manuscript submitted to *Quart. J. Roy. Meteor. Soc.*) showed that convective circulations derive momentum fluxes from the Coriolis force. In the presence of the NCT, convective circulations are tilted westward. This is the source of vertical fluxes of zonal momentum. In the linear case, Biello et al. (2024, manuscript submitted to *Quart. J. Roy. Meteor. Soc.*) were able to reduce the vertical flux convergence of zonal momentum from convection under the influence of the NCT to a simple function of a *filling fraction* of convection, the latitude, the diabatic heating magnitude, the height of heating, and the ratio of the rotation rate of Earth to the damping time scale. Such a simple function not only represents an easy parameterization in a global model but also implies understandable physics. Here, we generalize these results to the nonlinear case and compute the flux convergence for a range of damping regimes. While we are unable at present to provide analytical expressions for the flux convergence, we are able to extend the results to a much wider range of relevant dynamical scaling regimes, including when the effect of damping is weak, which is a singular limit in the linear case.

The primary results of this work may be summarized by the following three statements:

1) The most notable features of the two-component (i.e., poloidal/rotation induced) flow structure associated with convection under the influence of the full Coriolis force are preserved when nonlinear effects are retained as well as across a multitude of damping and diffusive regimes. The DoNUT framework for convective parameterization (Igel and Biello 2020) provides the most natural and comprehensive means by which to understand and quantify this behavior.
2) The nonlinear counterparts of the induced horizontal circulation computed by Biello et al. (2024, manuscript submitted to *Quart. J. Roy. Meteor. Soc.*) show that the NCT forces a westward tilt in convection across all relevant scaling regimes.
3) The westward tilt of subgrid-scale convection drives a vertical shear on larger scales. This shear may be a fundamental mechanism responsible for certain elements of large-scale tropical dynamics (see e.g., Seiki and Takayabu 2007a,b, for a discussion of the westerly wind burst structure of intraseasonal oscillations).

The layout of this paper is as follows. In section 2, we derive an asymptotic model for a nonlinear convective circulation driven by a steady diabatic heat source in the presence of the full Coriolis force using the DoNUT framework. In section 3, solutions are computed for a prescribed heat source, and the two-component structure of the flow is analyzed for a variety of damping regimes. In section 4, the upscale flux convergence of momentum is computed and discussed. Conclusions are drawn in section 5.

2. The asymptotic model for nonlinear circulations induced by diabatic heating

The starting point for our analysis are the steady, three-dimensional, nonlinear, Boussinesq equations on an f plane (see e.g., Vallis 2017, section 2.4) for the velocity field $\mathbf{v} = (u^x, v^y, w)^{\mathrm{T}}$, perturbation pressure field p, and buoyancy perturbation b, given by

$$\begin{aligned} (\mathbf{v}\cdot\nabla)\mathbf{v} + 2\boldsymbol{\Omega}\times\mathbf{v} &= -\nabla p + b\hat{\mathbf{z}} - \mathcal{D}\mathbf{v}, \\ \nabla\cdot\mathbf{v} &= 0, \\ (\mathbf{v}\cdot\nabla)b + N^2 w &= S. \end{aligned} \tag{2}$$

The equations of motion in Eq. (2) are considered within the standard Cartesian coordinate system $\mathbf{x} = (x, y, z)^{\mathrm{T}}$, so that the gradient operator is given by $\nabla = (\partial_x, \partial_y, \partial_z)$. Here, N is the buoyancy frequency, $\boldsymbol{\Omega}$ is the angular velocity vector of Earth, and $S = S(\mathbf{x})$ is a diabatic heat source representing the latent heat release as moisture in the atmosphere condenses. The right-hand side of the momentum equation in Eq. (2) contains a linear diffusion operator $\mathcal{D}$ defined as

$$\mathcal{D} = d(z) - \nu\nabla^2, \tag{3}$$

where $d(z)$ is a height-dependent Newtonian damping coefficient and ν is the eddy viscosity. A more thorough discussion of damping and diffusion is postponed until the end of this

Brought to you by UNIVERSITY OF CALIFORNIA Davis - SERIALS RECORDS SECTION | Unauthenticated | Downloaded 07/14/25 03:45 PM UTC

section. It is important to recognize that in a model primarily intended for realistic simulations, we would expect temporal variations at the convective scale and as such would need to include time derivatives in Eq. (2). Since our model is intended more as a theoretical exposition of the underlying structures associated with convective circulations, we are satisfied with omitting temporal variations a priori and understanding that they are of secondary importance for our purposes.

The key novelty in our problem is the presence of the NCT, so that the Coriolis force takes the form

$$-2\boldsymbol{\Omega}\times\mathbf{v} = (2\Omega v^y \sin\lambda - 2\Omega w\cos\lambda)\hat{\mathbf{x}} - 2\Omega u^x \sin\lambda\hat{\mathbf{y}} + 2\Omega u^x\cos\lambda\hat{\mathbf{z}} \tag{4}$$

in the Cartesian basis, where Ω is Earth's rotation rate and λ is the latitude. The TCTs are those proportional to $\sin\lambda$, and it is generally accepted that in most large-scale geophysical scenarios, they are the dominant terms since $|w| \ll |v^y|$ and the terms corresponding to hydrostatic balance supersede rotation in the vertical momentum equation (Holton 2004, section 1.2). However, on the convective scale, it is not so simple to disregard the NCT (i.e., those terms proportional to $\cos\lambda$), since the vertical and horizontal extent of a convective circulation are of the same order, and hydrostatic balance does not necessarily hold in the vertical momentum equation. Moreover, in the vicinity of the equator when $|\lambda| \ll 1$, we have that $\cos\lambda \sim 1$ while $\sin\lambda \ll 1$, indicating that the NCT could indeed play an important role within the tropics in particular.

Given that we are motivated by convective circulations associated with cumulonimbus clouds, we nondimensionalize system (2) according to the scalings:

$$\mathbf{x} = H\mathbf{x}^*, \qquad \mathbf{v} = \frac{H}{T}\mathbf{v}^*, \qquad p = \frac{H^2}{T^2}p^*,$$
$$b = \frac{H}{T^2}b^*, \qquad S = \frac{N^2H}{T}S^*, \qquad d(z) = \frac{1}{T}d^*(z), \tag{5}$$

where H is the tropopause height, T is the overturning time scale for the convective circulation, and variables with asterisks denote the nondimensional counterparts to the dimensional variables. For typical values of $H = 15$ km and $T = 1200$ s, the velocity scale for the circulation is $W_{\max} = H/T \approx 12.5$ m s^{-1}, which is an appropriate speed for a strong updraft associated with a tropical cumulonimbus cloud. While we have chosen to scale the damping coefficient $d(z)$ using the advective time scale T^{-1}, we recognize that this is not necessarily appropriate through the entire troposphere but is rather a measure of the dominant damping effects which are found near the boundary layer.

The nondimensional equations (dropping asterisks for simplicity) are then given by

$$(\mathbf{v}\cdot\nabla)\mathbf{v} + \frac{1}{\mathrm{Ro}}\hat{\mathbf{N}}\times\mathbf{v} = -\nabla p + b\hat{\mathbf{z}} - \mathcal{D}\mathbf{v},$$
$$\nabla\cdot\mathbf{v} = 0,$$
$$\mathrm{Fr}^2(\mathbf{v}\cdot\nabla)b + w = S, \tag{6}$$

where the nondimensional parameters Ro (Rossby number) and Fr (Froude number) are given by

$$\mathrm{Ro} = \frac{1}{2\Omega T}, \qquad \mathrm{Fr} = \frac{1}{TN}, \tag{7}$$

and $\hat{\mathbf{N}} = \cos\lambda\hat{\mathbf{y}} + \sin\lambda\hat{\mathbf{z}}$ is the unit vector which points in the direction of the North Star. For typical values $T \approx 1200$ s, $N = 0.02$ s^{-1}, and $2\Omega = 1.4\times10^{-4}$ s^{-1}, we find $\mathrm{Ro}^{-1} \approx 0.17$ and $\mathrm{Fr}^2 \approx 1.7\times10^{-3}$. Importantly, for any reasonable scales associated with a cumulonimbus cloud, the parameters obey $\mathrm{Fr}^2 \ll \mathrm{Ro}^{-1}$, and hence we are able to set $\mathrm{Fr} = 0$ so that $w = S$. This approximation, namely, the *weak temperature gradient* (WTG) approximation, is in some sense a universal law for cumulus convection in the tropics, as it holds strongly across all relevant overturning time scales (Held and Hoskins 1985; Sobel et al. 2001; Klein 2010).

a. Large Rossby number asymptotics

Given an axisymmetric heat source $S = S(r, z)$, where $(r, \theta, z)^{\mathrm{T}}$ are the usual cylindrical polar coordinates, we take the curl of the momentum equation in Eq. (6) to obtain the vorticity equation. In the polar coordinate basis, where $\hat{\mathbf{r}} = (\cos\theta, \sin\theta, 0)^{\mathrm{T}}$ and $\hat{\boldsymbol{\theta}} = (-\sin\theta, \cos\theta, 0)^{\mathrm{T}}$, this yields

$$(\mathbf{v}\cdot\nabla)\boldsymbol{\omega} - (\boldsymbol{\omega}\cdot\nabla)\mathbf{v} - \frac{1}{\mathrm{Ro}}\hat{\mathbf{N}}\cdot\nabla\mathbf{v} = \frac{1}{r}\frac{\partial b}{\partial\theta}\hat{\mathbf{r}} - \frac{\partial b}{\partial r}\hat{\boldsymbol{\theta}} - \mathcal{D}\boldsymbol{\omega} - d'(z)\hat{\mathbf{z}}\times\mathbf{v}, \tag{8}$$

where $\boldsymbol{\omega} = \nabla\times\mathbf{v}$ is the vorticity vector and $d'(z)$ is the derivative of $d(z)$. In cylindrical polar coordinates, the components of velocity and vorticity are given by $\mathbf{v} = u\hat{\mathbf{r}} + v\hat{\boldsymbol{\theta}} + w\hat{\mathbf{z}}$ and $\boldsymbol{\omega} = \omega^r\hat{\mathbf{r}} + \omega^\theta\hat{\boldsymbol{\theta}} + \omega^z\hat{\mathbf{z}}$, respectively, while the gradient operator is written as $\nabla = \hat{\mathbf{r}}\partial_r + \hat{\boldsymbol{\theta}}r^{-1}\partial_\theta + \hat{\mathbf{z}}\partial_z$. We recall that the vertical velocity field is determined explicitly by the form of the heating due to the WTG equation

$$w = S(r, z) \tag{9}$$

and hence is itself an axisymmetric function—identical to the heat source in nondimensional terms.

For strongly nonlinear circulations, we consider the Rossby number to be large (for an overturning time of $T \approx 1200$ s we find $\mathrm{Ro} \approx 6.0$, though we note that for shorter overturning times, Ro may be even larger). Hence, with $\mathrm{Ro}^{-1} \ll 1$, the form of the solution to Eq. (8) may be sought approximately by making the substitutions:

$$\mathbf{v} \to \mathbf{v} + \frac{1}{\mathrm{Ro}}\mathbf{V}, \qquad \boldsymbol{\omega} \to \boldsymbol{\omega} + \frac{1}{\mathrm{Ro}}\boldsymbol{\Lambda}, \qquad b \to b + \frac{1}{\mathrm{Ro}}B, \tag{10}$$

where lowercase variables correspond to the nonrotating *poloidal* circulation and uppercase variables correspond to the flow *induced* by the Coriolis force. The above substitutions [Eq. (10)] constitute a two-term regular perturbation expansion for the velocity, vorticity, and buoyancy fields, correct up to $O(\mathrm{Ro}^{-2})$; however, it should be noted that the approximation may be straightforwardly extended to higher orders of accuracy.

Since the heat source $S(r, z)$ is axisymmetric, the velocity field $\mathbf{v}$ is itself an axisymmetric function, whose azimuthal

Brought to you by UNIVERSITY OF CALIFORNIA Davis - SERIALS RECORDS SECTION | Unauthenticated | Downloaded 07/14/25 03:45 PM UTC

component vanishes. Thus, we are able to introduce the poloidal streamfunction (also known as the Stokes streamfunction) $\psi(r, z)$ satisfying

$$u = -\frac{1}{r}\frac{\partial \psi}{\partial z}, \qquad w = \frac{1}{r}\frac{\partial \psi}{\partial r}, \tag{11}$$

where the poloidal vorticity $\boldsymbol{\omega}$ satisfies

$$\boldsymbol{\omega} = \omega^{\theta}\hat{\boldsymbol{\theta}} = \left(\frac{\partial u}{\partial z} - \frac{\partial w}{\partial r}\right)\hat{\boldsymbol{\theta}} = -\frac{1}{r}\left(\frac{\partial^2 \psi}{\partial r^2} - \frac{1}{r}\frac{\partial \psi}{\partial r} + \frac{\partial^2 \psi}{\partial z^2}\right)\hat{\boldsymbol{\theta}}. \tag{12}$$

The WTG equation allows us to specify the poloidal streamfunction uniquely from the heat source via the integral

$$\psi(r, z) = -\int_r^{\infty} S(r', z) r' dr', \tag{13}$$

and hence the poloidal component of the vorticity ω^{θ} is determined from Eq. (12). The lowest order buoyancy may be determined from the azimuthal component of the vorticity equation via the integral

$$b(r, z) = \int_r^{\infty} \hat{\boldsymbol{\theta}} \cdot \mathcal{D}\boldsymbol{\omega} + \frac{d'(z)\psi_z - \nabla^{\perp}\psi \cdot \nabla\omega^{\theta}}{r'} dr', \tag{14}$$

where the skew-gradient operator is defined as $\nabla^{\perp} = (\partial_z, 0, -\partial_r)^{\mathrm{T}}$. Equations (11)–(14) constitute a set of diagnostic relations specifying the *poloidal circulation variables* (PCVs hereafter) in terms of the heat source $S(r, z)$.

At order $O(\mathrm{Ro}^{-1})$, the equation for the induced vorticity $\boldsymbol{\Lambda} = (\Lambda^r, \Lambda^{\theta}, \Lambda^z)^{\mathrm{T}}$ is given by

$$\begin{aligned}(\mathbf{v} \cdot \nabla)\boldsymbol{\Lambda} + (\mathbf{V} \cdot \nabla)\boldsymbol{\omega} - (\boldsymbol{\omega} \cdot \nabla)\mathbf{V} - (\boldsymbol{\Lambda} \cdot \nabla)\mathbf{v} - \hat{\mathbf{N}} \cdot \nabla\mathbf{v} \\ = \frac{1}{r}\frac{\partial B}{\partial \theta}\hat{\mathbf{r}} - \frac{\partial B}{\partial r}\hat{\boldsymbol{\theta}} - \mathcal{D}\boldsymbol{\Lambda} - d'(z)\hat{\mathbf{z}} \times \mathbf{V}.\end{aligned} \tag{15}$$

Notably, since the WTG equation gives a perfect balance between the poloidal component of the vertical velocity field and the heating, the induced velocity field must contain no vertical component and lie entirely within the r–θ plane, i.e., $\mathbf{V} = (U, V, 0)^{\mathrm{T}}$. Therefore, we introduce a streamfunction Ψ for the induced flow which satisfies

$$U = \frac{1}{r}\frac{\partial \Psi}{\partial \theta}, \qquad V = -\frac{\partial \Psi}{\partial r}, \tag{16}$$

from which it is found that the induced vorticity may be written as

$$\boldsymbol{\Lambda} = \partial_{rz}^2 \Psi\hat{\mathbf{r}} + \frac{1}{r}\partial_{\theta z}^2 \Psi\hat{\boldsymbol{\theta}} - \nabla_h^2 \Psi\hat{\mathbf{z}}, \tag{17}$$

where $\nabla_h^2 = \partial_{rr}^2 + r^{-1}\partial_r + r^{-2}\partial_{\theta\theta}^2$ is the horizontal Laplacian differential operator.The vertical component of Eq. (15), which is simplified by the fact that $\mathbf{V}$ and $\boldsymbol{\omega}$ contain no vertical components, is given by

$$\begin{aligned}(u\partial_r + w\partial_z)\nabla_h^2 \Psi + w_r \Psi_{rz} - w_z \nabla_h^2 \Psi + \mathcal{D}\nabla_h^2 \Psi \\ = -w_r \sin\theta \cos\lambda - w_z \sin\lambda\end{aligned} \tag{18}$$

and is sufficient to determine the induced streamfunction Ψ. Equation (18) is the primary result of this work, although it is somewhat difficult to interpret physically. The first and fourth terms describe the advection (by the poloidal flow) and diffusion of the vertical component of the induced vorticity. The third term describes the stretching of the vertical component of the induced vorticity by an increasing vertical velocity. The second term describes the bending of the horizontal (axial) component into the vertical component of the induced vorticity by the axial shear of the vertical component of the poloidal flow. The right-hand side is the forcing provided by the Coriolis terms and provides the coupling between the leading-order poloidal circulation and the induced flow. In essence, the asymptotic theory employed in this paper has reduced the nonlinear circulation problem into a two-step process whereby we first find the poloidal circulation from a given heating and then solve a relatively simple linear PDE to determine the effect of rotation at next order.

b. *The diffusion operator*

Thus far, the diffusion operator $\mathcal{D}(z)$, the dimensional form of which was given in Eq. (3), has received little attention beyond its decomposition into linear Newtonian drag and eddy viscosity components. To fully appreciate the physics involved with our model, an appropriately detailed discussion of the diffusion operator and its effect on the circulation must be given.

It is perhaps best to initiate such a discussion by recognizing that diffusion is not merely an additional feature of our model but rather a necessity. Indeed, it may be seen that after omitting nonlinear effects from Eq. (18), a solution does not exist in the absence of diffusion. In other words, diffusion is vital in maintaining a steady convective circulation in the presence of rotation. This is effectively the argument made in the linear regime by Marsico et al. (2023) that "the vertical torque due to the Coriolis force acting on the convective circulation must be in balance with the torque associated with vorticity damping."In a nondimensional form, the diffusion operator becomes

$$\mathcal{D} = d(z) - \frac{1}{\mathrm{Re}}\nabla^2, \tag{19}$$

where $\mathrm{Re} = W_{\max}H/\nu$ is a Reynolds number measuring the ratio of the inertial forces in the circulation to the diffusion by eddy viscosity. In the above decomposition, $d(z)$ is the dimensionless, height-dependent coefficient of Newtonian drag and the Laplacian operator corresponds to a simple parameterization of momentum dissipation via turbulence (see e.g., Taylor 1959, for a historical account). We choose $d(z)$ of the form

$$d(z) = d_0 \exp(-z^2/\gamma^2), \tag{20}$$

where d_0 is a constant controlling the magnitude of the damping at the ground and γ is a parameter controlling the rate at which damping decays with increasing height.

One limit of interest—termed the *homogenous Newtonian damping* (HND) limit, is found by taking $\gamma \to \infty$ and $\mathrm{Re} \to \infty$, so that $\mathcal{D} \equiv d_0$. This form of diffusion, comprised solely of a

Brought to you by UNIVERSITY OF CALIFORNIA Davis - SERIALS RECORDS SECTION | Unauthenticated | Downloaded 07/14/25 03:45 PM UTC

vertically homogenous Newtonian damping, is somewhat lacking in its physical realism; however, due to the already idealized physics associated with our simplified model, it is worthwhile investigating a case of minimal mathematical complexity. Moreover, this case allows us to most easily draw direct comparisons to the prior work of Marsico et al. (2023, 2024), who solve the linear system in the HND limit. With a constant damping of this form, the strength of the diffusion term is controlled entirely by the constant d_0, and the dimensional coefficient of the damping is given by d_0/T. For characteristic overturning time scale $T = 1200$ s and taking $d_0 = 1.5$, the dimensional damping coefficient is $d_0/T \approx 1.3 \times 10^{-3}$ s^{-1}, which lies firmly between the weak (10^{-5} s^{-1}) and strong (10^{-1} s^{-1}) damping limits considered by Marsico et al. (2024).

In general, we will consider the case where γ is finite in Eq. (20), which we term the *enhanced boundary layer damping* (EBLD) limit. The upshot of this parameter regime is that the height dependence in $d(z)$ allows us to model the enhanced damping effects in the lower troposphere caused by the atmospheric boundary layer. Indeed, it is well understood that turbulent effects are much more pronounced within the boundary layer than in the midtroposphere and that a realistic damping parameterization can have major implications on models of deep convection and hurricane development (see e.g., Montgomery et al. 2001; Smith and Vogl 2008; Smith and Montgomery 2010; Smith et al. 2014).

In conjunction with the height dependence in the Newtonian damping $d(z)$, we must also take $\mathrm{Re}^{-1} > 0$. Our reasons for including eddy viscosity are twofold. First, from a physical standpoint, it allows us to include the effects of isotropic "background" turbulence alongside the enhanced diffusion parameterization within the boundary layer. This, again, calls back to the prior work of Marsico et al. (2024) who study the linear model with eddy viscosity. The second (arguably less satisfactory) reason is that the Laplacian operator acts to smooth the solutions to Eq. (18), so as to avoid numerical instability in later calculations. In essence, the inclusion of eddy viscosity forces Eq. (18) to be elliptic over the entire domain and allows for easy inversion of the differential operator. With this in mind, whenever we consider the EBLD regime, we use a value of $\mathrm{Re} = 200$, so that the effects of eddy viscosity do not obscure the other more relevant features of the model. For an overturning time scale of $T = 1200$ s and $H = 15$ km, the dimensional eddy viscosity is $\nu \approx 938$ m^2 s^{-1}, which is a reasonable estimate in the atmosphere—particularly in regions of high convective activity. Note that we are assuming an isotropic eddy viscosity, which may not necessarily be the most realistic model. Such an assumption is easily relaxed; however, we opt to ignore this possibility in favor of simplicity.

3. The poloidal and induced components of the convective circulation

In section 2, we derived a system of equations—the solutions of which (consisting of the PCV and the induced streamfunction Ψ) form a two-term approximation for the nonlinear circulation driven by an axisymmetric heat source under the influence of both the TCT and NCT. This section is concerned with providing a numerical solution to this system. In principle, this task is as simple as computing the PCV from the given heat source and inverting Eq. (18); however, thus far, we have left our discussion of the relevant physics intentionally vague so as to keep the mathematical analysis as general as possible. It is arguably a more difficult task, therefore, to fully present our solutions in a way which sheds light on the underlying physical principles at hand, while maintaining a coherent and satisfactory argument in favor of our model. So as to properly discuss these solutions, while drawing parallels and contrasts to those studies preceding this work, we subdivide this section as follows:

1) We begin with a discussion of the axisymmetric heat source $S(r, z)$ and give an explicit functional form to be used in calculations henceforth. We further compute the PCV from the WTG approximation and Eqs. (11)–(14).
2) We describe a solution method for Eq. (18) allowing for its decomposition into equations governing the TCT and NCT induced components of Ψ. We solve these subsequent equations in both the linear and nonlinear cases across three relevant damping and diffusion regimes.
3) A detailed discussion of the solutions for the induced streamfunction Ψ is given, with a particular focus upon the component induced by the NCT.
4) We construct the streamlines for the full three-dimensional convective circulation in the presence of both the TCT and NCT and provide elucidating figures illustrating our results.

Throughout this section, we draw comparisons wherever possible to those studies preceding and motivating this work, particularly those of Marsico et al. (2023, 2024).

a. Diabatic heating and the poloidal circulation

Motivated by the fact that the WTG approximation holds for the poloidal circulation, i.e., $w(r, z) = S(r, z)$, we choose a functional form for the heating

$$S(r, z) = S_\alpha(r)\sin(\pi z), \tag{21}$$

where

$$S_\alpha(r) = (1 - \alpha r^2)\exp(-\alpha r^2), \tag{22}$$

and α is a parameter controlling the horizontal extent of the heating (and cooling) regions.

Importantly, this heating profile (and consequently the vertical velocity) vanishes at the ground $z = 0$ and the tropopause $z = 1$ and is maximal in the midtroposphere $z = 1/2$ at $r = 0$ (the center of the circulation). This form of heating is analogous to those functional forms used in the study of hurricane development (see, e.g., Schubert and Hack 1982; Hack and Schubert 1986; Schubert and Alworth 1987; Smith and Montgomery 2016). In addition to this, $S_\alpha(r)$ satisfies the property

$$\int_0^\infty S_\alpha(r)\, r dr = 0, \tag{23}$$

so that there is no net heating or cooling introduced into the system through the heat source. This is a particularly

Brought to you by UNIVERSITY OF CALIFORNIA Davis - SERIALS RECORDS SECTION | Unauthenticated | Downloaded 07/14/25 03:45 PM UTC

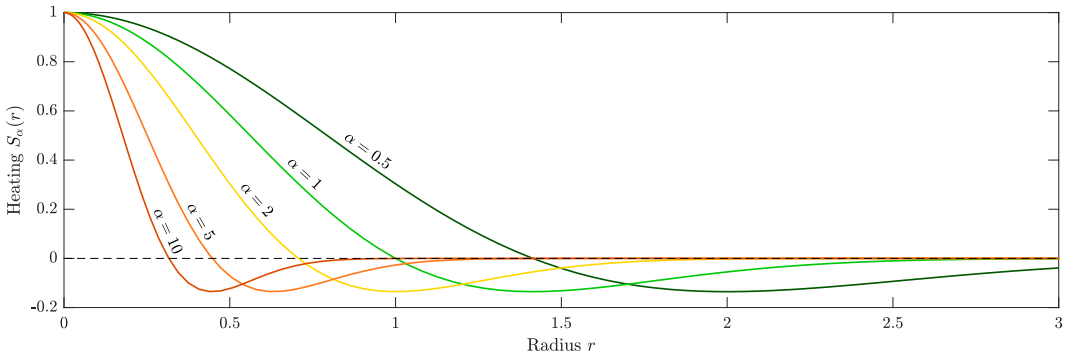

FIG. 1. Radial heating profile $S_\alpha(r)$ for various values of α.

important requirement since we wish to model a steady-state convective circulation which would in principle be reasonable in the absence of diffusion. While it is possible to achieve steady-state solutions with a net source/sink of buoyancy in the system, such solutions require that excess buoyancy is removed via either turbulence or viscous diffusion. Such processes are of secondary importance for our purposes, and hence we treat Eq. (23) as a necessary condition for our model.

Figure 1 shows plots of $S_\alpha(r)$ for various values of α. We see that the radial heating profile consists of a region of heating maximized at $r = 0$, followed by a much less intense region of cooling (with approximately equal radial extent). In particular, for $\alpha = 5$, we see that $S_5(r)$ vanishes at approximately $r = 0.42$, so that the horizontal extent of the positive heating is approximately equal to the height of the tropopause. This corresponds to an aspect ratio ≈1 convective circulation and henceforth will be the radial heating profile we use in calculations. For the sake of simplicity, we will denote $S_5(r)$ as $s(r)$ from hereon.

With the heat source $S(r, z)$ (and hence the vertical velocity w) specified, it is straightforward to determine the PCV streamfunction $\psi(r, z)$, radial velocity $u(r, z)$, and azimuthal vorticity $\omega^\theta(r, z)$ from Eqs. (11) to (13) as

$$\psi(r, z) = \sin(\pi z)\int_0^r s(r')r'\,dr' = \frac{\sin(\pi z)}{2}r^2\exp(-5r^2), \tag{24}$$

$$u(r, z) = -\frac{\pi\cos(\pi z)}{r}\int_0^r s(r')r'\,dr' = -\frac{\pi\cos(\pi z)}{2}r\exp(-5r^2), \tag{25}$$

$$\begin{aligned}\omega^\theta(r, z) &= \frac{\sin(\pi z)}{r}\left[-rs'(r) + \pi^2\int_0^r s(r')r'\,dr'\right]\\ &= \sin(\pi z)r\left(20 + \frac{\pi^2}{2} - 50r^2\right)\exp(-5r^2).\end{aligned} \tag{26}$$

Figure 2 shows numerical solutions for the poloidal streamfunction, radial component of velocity, and vorticity for the heat source $S(r, z) = s(r)\sin(\pi z)$. The results appear to simulate the motion of a convective circulation in an irrotational atmosphere, at least qualitatively. Taking the tropopause to be at $H = 15$ km and the convective overturning time as $T = 1200$ s, we see a circulation with strong updrafts concentrated

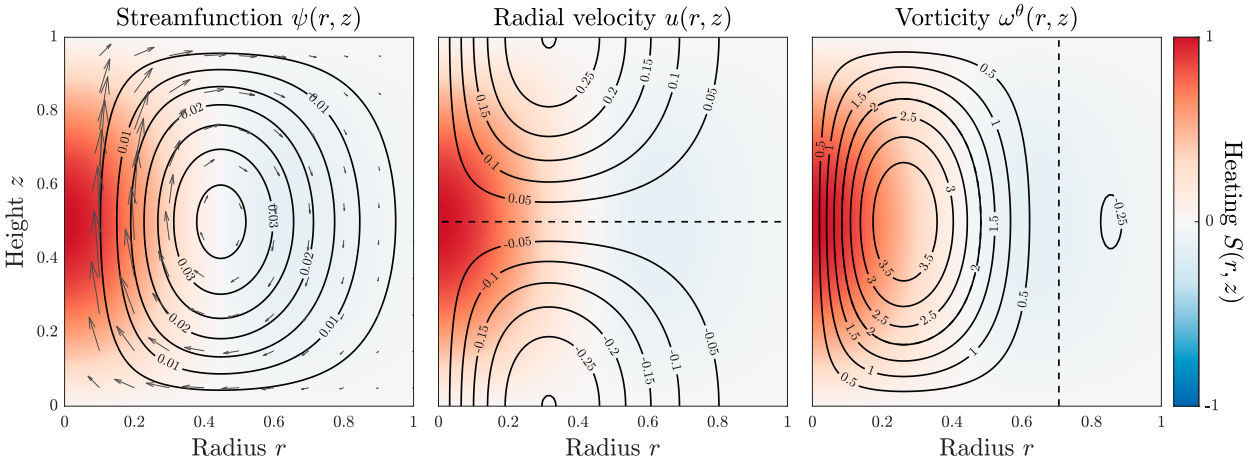

FIG. 2. Contours for the PCV streamfunction $\psi(r, z)$, radial velocity $u(r, z)$, and azimuthal vorticity $\omega^\theta(r, z)$ computed from Eqs. (24)–(26). The heating $S(r, z) = s(r)\sin(\pi z)$ is shown in color, while arrows indicating the direction and strength of the poloidal flow are included in the first panel along with the streamfunction. Zero contours are shown with dashed lines.

Brought to you by UNIVERSITY OF CALIFORNIA Davis - SERIALS RECORDS SECTION | Unauthenticated | Downloaded 07/14/25 03:45 PM UTC

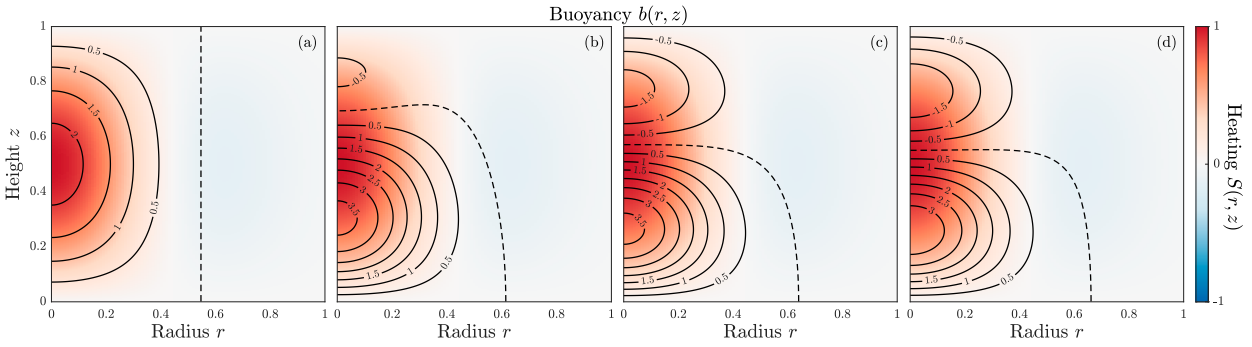

FIG. 3. Contours for the PCV buoyancy $b(r, z)$. (a),(b) The linear and nonlinear circulation in the HND limit, respectively, and (c),(d) the nonlinear circulation in the EBLD regime with Re = 200 and Re $\to \infty$, respectively. The diabatic heating $S(r, z) = s(r)\sin(\pi z)$ is shown in color, and zero contours are shown with dashed lines. In all cases, the coefficient of Newtonian damping is given by $d_0 = 1.5$.

near the center of the heat source (maximum updraft speed $W_{\max} = 12.5\ \mathrm{m\ s^{-1}}$), with a much broader and weaker downwelling region outside (maximum downwelling speed $\approx 1.6\ \mathrm{m\ s^{-1}}$). The radial velocity profile $u(r, z)$ is antisymmetric about the midtroposphere, with maximum dimensional magnitude of $\approx 3.8\ \mathrm{m\ s^{-1}}$ at the tropopause and ground, a distance of approximately $0.3 \times H \approx 4.5$ km from the convective core (the center of the updraft region). The vorticity is positive over most of the domain with a maximum dimensional value of $3.3 \times 10^{-3}\ \mathrm{s^{-1}}$ at a distance of approximately 3.8 km from the convective core. Due to Eq. (23) and the fact that cooling is necessary, the vorticity vanishes approximately 10.5 km from the convective core, followed by a region where it is small in magnitude and negative.

Notably, the only PCV quantity affected by either the diffusion operator or the nonlinearity is the buoyancy $b(r, z)$. Figure 3 shows plots of the PCV buoyancy in four different cases. First, Fig. 3a shows the buoyancy calculated in the HND limit in the absence of nonlinearity, in which case

$$b(r, z) = d_0 \int_r^\infty \omega^\theta(r', z)dr' = d_0 \sin(\pi z)\left(1 + \frac{\pi^2}{20} - 5r^2\right)\exp(-5r^2). \tag{27}$$

Naturally, we see that the flow retains symmetry about the midtroposphere, with a region of positive buoyancy concentrated at the convective core and extending radially outward to approximately 8.25 km. For $H = 15$ km and $T = 1200$ s, the maximum dimensional value of the buoyancy is approximately $2.3 \times 10^{-2}\ \mathrm{m\ s^{-2}}$. Figure 3b shows the equivalent version of the PCV buoyancy calculated from the nonlinear circulation. Interestingly, the symmetry about the midtroposphere is broken, even in the HND limit. We see that the nonlinear advection of vorticity draws heavier air in from the outer domain, creating a small region of negative buoyancy at the top of the convective core. Furthermore, the magnitude of the positive buoyancy region is much greater than in the linear case, with a maximum dimensional value of approximately $3.7 \times 10^{-2}\ \mathrm{m\ s^{-2}}$. Figures 3c and 3d, which are both calculated from a nonlinear circulation in the EBLD regime, show that using a Newtonian damping that decreases with height exacerbates the effect that the vorticity advection has in the upper troposphere. We see that the region of negative buoyancy is much more pronounced and occupies the majority of the upper troposphere. The maximum negative value of the buoyancy occurs approximately 12 km above the ground and has a dimensional value of approximately $1.7 \times 10^{-2}\ \mathrm{m\ s^{-2}}$. Furthermore, a comparison of Fig. 3c (calculated using Re = 200) with Fig. 3d (calculated in the absence of eddy viscosity) shows that the poloidal flow is only marginally affected by eddy viscosity at this small of a magnitude, with the qualitative characteristics entirely unaltered.

The PCV solutions computed above are a concrete example of the DoNUT model introduced by Igel and Biello (2020)—a proposed alternative model for convection in the atmosphere. The key insight that the DoNUT provides is that by retaining the essential circulatory features of the poloidal circulation associated with convection, the atmospheric response to forcing, and the resulting fluxes are built directly into the model. However, Igel and Biello artificially construct a DoNUT circulation to examine the net force introduced by the NCT; here, we have found that such DoNUTs arise naturally from a properly constructed convective model—in this case, as the leading order poloidal flow in a nonlinear, axisymmetric convective circulation. An analogous model involving a DoNUT-like circulation was independently proposed by Goldsmith and Esler (2023), albeit in a different scaling regime where the WTG approximation does not apply.

b. *Solution to Eq. (18)*

With the PCV streamfunction ψ, vorticity ω^θ, and buoyancy b determined in terms of the diabatic heat source, we are able to turn our attention to Eq. (18) for the induced streamfunction $\Psi(r, \theta, z)$. Since the PCVs are axisymmetric, and since the diffusion operator consists of a damping term which depends only on height and a fully isotropic eddy viscosity term, it is straightforward to see that Ψ must have a relatively simple dependence on both the azimuthal coordinate and latitude. Therefore, the problem is greatly simplified by realizing that Ψ may be separated as

$$\Psi(r, \theta, z) = \sin\lambda\Psi^T(r, z) + \sin\theta\cos\lambda\Psi^N(r, z), \tag{28}$$

Brought to you by UNIVERSITY OF CALIFORNIA Davis - SERIALS RECORDS SECTION | Unauthenticated | Downloaded 07/14/25 03:45 PM UTC

where $\Psi^T(r, z)$ and $\Psi^N(r, z)$ are the functional profiles of the induced streamfunction in the r–z plane driven by the traditional and nontraditional components of the Coriolis force, respectively.

Upon substituting Eq. (28) into Eq. (18), we arrive at a pair of axisymmetric equations:

$$(u^r\partial_r + w\partial_z)\Lambda^T - w_z\Lambda^T - w_r\partial^2_{rz}\Psi^T + d(z)\Lambda^T - \frac{1}{\mathrm{Re}}\left(\partial^2_{rr} + \frac{1}{r}\partial_r + \partial^2_{zz}\right)\Lambda^T = w_z, \tag{29}$$

$$(u^r\partial_r + w\partial_z)\Lambda^N - w_z\Lambda^N - w_r\partial^2_{rz}\Psi^N + d(z)\Lambda^N - \frac{1}{\mathrm{Re}}\left(\partial^2_{rr} + \frac{1}{r}\partial_r - \frac{1}{r^2} + \partial^2_{zz}\right)\Lambda^N = w_r, \tag{30}$$

where

$$\Lambda^T(r, z) = -\frac{1}{r}\partial_r(r\partial_r\Psi^T) \quad \text{and}$$
$$\Lambda^N(r, z) = -\frac{1}{r}\partial_r(r\partial_r\Psi^N) + \frac{\Psi^N}{r^2} \tag{31}$$

are the traditional and nontraditional profiles of the induced vertical component of vorticity, i.e.,

$$\hat{\mathbf{z}}\cdot\boldsymbol{\Lambda}(r, \theta, z) = -\nabla^2_h\Psi = \sin\lambda\Lambda^T(r, z) + \sin\theta\cos\lambda\Lambda^N(r, z). \tag{32}$$

Equations (29) and (30) together with Eq. (31) constitute a linear system of two-dimensional PDEs, which may be inverted to find $\{\Lambda^T(r, z), \Lambda^N(r, z), \Psi^T(r, z), \Psi^N(r, z)\}$. In the linear problem, the vertical structure of all induced variables is prescribed by the vertical structure of the poloidal flow—in fact, the NCT component of the induced flow satisfies no-slip boundary conditions, while the TCT component satisfies free-slip boundary conditions. In the nonlinear problem, however, we have the freedom to choose appropriate conditions at the upper and lower troposphere, which on the scales relevant to this work are free slip, i.e.,

$$\partial_z\Psi^T = \partial_z\Psi^N = 0 \quad \text{on} \quad z = 0, 1, \tag{33}$$

while at the convective core, the conditions which ensure smooth and continuous solutions are

$$\partial_r\Psi^T = \Psi^N = 0 \quad \text{on} \quad r = 0. \tag{34}$$

As well as the boundary conditions, we must also prescribe decay conditions far from the heat source:

$$\Lambda^T, \Psi^T, \Lambda^N, \Psi^N \to 0 \quad \text{as} \quad r \to \infty. \tag{35}$$

In numerical calculations where the behavior at infinity is approximated by applying an artificial boundary far from the heat source, these decay conditions are replaced with Dirichlet conditions at the boundary.

Let us now consider a range of relevant parameter regimes associated with Eqs. (29)–(31) and the appropriate solution methods in each case.

1) Linear solutions

The papers of Marsico et al. (2023, 2024) give analytical solutions to the linear versions of Eqs. (29) and (30) in the HND limit as well as a numerical solution in the case where the diffusion consists solely of an eddy viscosity term. It is trivial to extend the analytical results into the linear EBLD regime in the absence of eddy viscosity ($\mathrm{Re} \to \infty$) via direct integration. When $S(r, z) = s(r)\sin(\pi z)$, we find for the vorticity and streamfunction induced by the TCT:

$$\Lambda^T(r, z) = \frac{\pi}{d(z)}s(r)\cos(\pi z), = \frac{\pi}{d(z)}(1 - 5r^2)\exp(-5r^2)\cos(\pi z), \tag{36}$$

$$\Psi^T(r, z) = -\frac{\pi}{d(z)}\cos(\pi z)\int_0^r\left[\frac{1}{r'}\int_0^{r'}s(r'')r''dr''\right]dr', = -\frac{\pi}{20d(z)}[1 - \exp(-5r^2)]\cos(\pi z), \tag{37}$$

and by the NCT

$$\Lambda^N(r, z) = \frac{1}{d(z)}s'(r)\sin(\pi z), = \frac{10r}{d(z)}(5r - 2)\exp(-5r^2)\sin(\pi z), \tag{38}$$

$$\Psi^N(r, z) = -\frac{1}{d(z)}\frac{\sin(\pi z)}{r}\int_0^r s(r')r'dr', = -\frac{r}{2d(z)}\exp(-5r^2)\sin(\pi z). \tag{39}$$

In general, it is not possible to find analytic solutions to the linear problem in the EBLD regime when the eddy viscosity is nonzero; however, for a constant Newtonian damping, one finds the solutions in the presence of eddy viscosity through the method of Green's functions, and quasi-analytic solutions are even possible in the full EBLD regime using Duhamel's principle. In practice, however, one would almost certainly prefer to solve these equations numerically, and thus we opt to omit these techniques from further discussion.

2) Nonlinear solutions

Nonlinear approximations are found via solutions to the quasi-linear equations in Eqs. (29) and (30), which in general must be found numerically. To do so, we first truncate the domain in the radial direction at a value $r = r_{\mathrm{out}}$ and apply a Chebyshev spectral collocation method (see e.g., Trefethen 2000; Boyd 2001) over the truncated domain $(r, z) \in [0, r_{\mathrm{out}}] \times [0, 1]$. Correspondingly, the decay conditions [Eq. (35)] are replaced with their equivalent boundary conditions on $r = r_{\mathrm{out}}$. The collocation method uses the command cheb.m (Trefethen 2000) with $N_r = 100$ and $N_z = 35$ basis functions in the radial and vertical directions, respectively. It is then straightforward to integrate the equations in three parameter regimes of interest:

(i) The strong Newtonian damping regime in the HND limit

In the absence of eddy viscosity, it is (perhaps surprisingly) possible to find convergent solutions for the NCT induced

Brought to you by UNIVERSITY OF CALIFORNIA Davis - SERIALS RECORDS SECTION | Unauthenticated | Downloaded 07/14/25 03:45 PM UTC

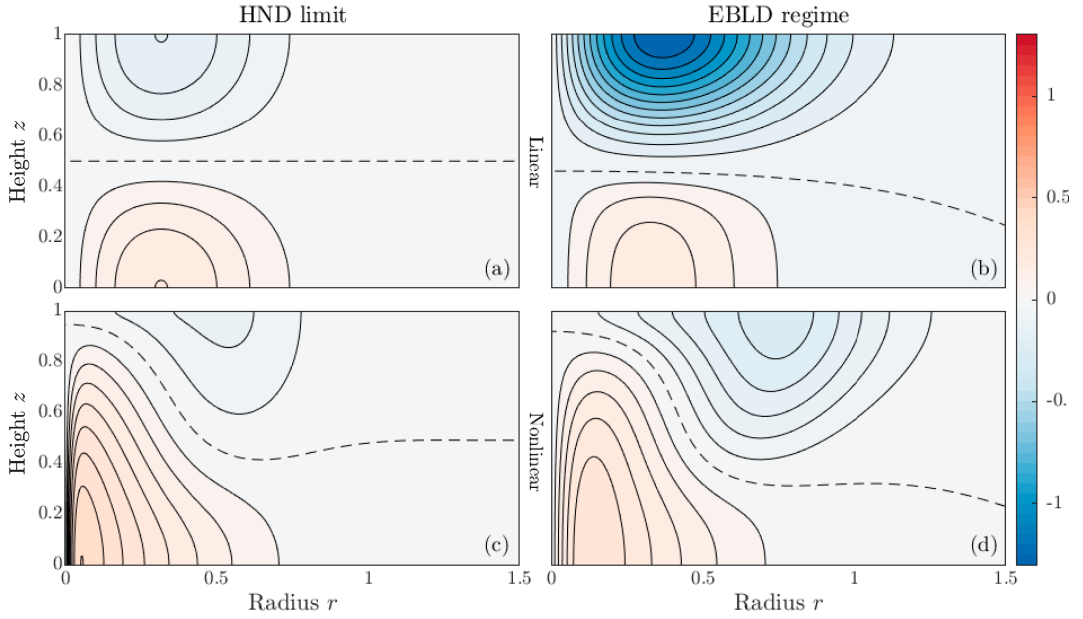

FIG. 4. Contour plots of the TCT induced azimuthal velocity $V^T(r, z) = -\partial_r \Psi^T(r, z)$. (a),(b) Linear solutions in the HND (with $d_0 = 1.5$) limit and EBLD (with $d_0 = 1.5$, Re = 200) regime, respectively, and (c),(d) the equivalent nonlinear solutions. Contours are shown at intervals of 0.05 except for in the negative region of (b) where contours are only shown at intervals of 0.1 for clarity. Dashed lines correspond to zero contours.

vorticity and streamfunction from Eq. (30), provided that the Newtonian damping coefficient d_0 remains relatively large. For the TCT induced quantities, however, numerically stable solutions may not be found unless we retain at least some diffusion via eddy viscosity. The reason for this discrepancy is not completely clear from our analysis, although the numerical experiments performed below indicate that diffusion by eddy viscosity is necessary to ensure that the gradient in azimuthal velocity is finite at the convective core, and that angular momentum is conserved. Consequently, when performing calculations in this regime, we set Re = 4000 in Eq. (29). For characteristic velocity and height scales $W_{\max} = 12.5$ m s^{-1} and $H = 15$ km, this corresponds to a dimensional eddy viscosity of $\nu \approx 47$ m^2 s^{-1} which, if it were being included on physical grounds, would be an exceedingly low estimate (Pedlosky 1987, section 4.2). In our calculations for this regime, we choose $d_0 = 1.5$.

The purpose of this regime is for direct comparison with the linear work of Marsico et al. (2023, 2024) in the HND limit. That is, we are able to see the effects of nonlinearity in isolation and free from the influence of complex diffusive phenomena.

(ii) The strong Newtonian damping and EBLD regime

In this regime, we retain the same value for the Newtonian damping at the ground but allow it to decay with height—we choose $d_0 = 1.5$ and $\gamma = 1/2$ in Eq. (20), so that near the tropopause, the damping is approximately 0.02 times its value at the ground. Due to the rapidly decaying damping, we must also retain the effects of eddy viscosity so that the solutions remain numerically stable. As previously discussed, we choose Re = 200, corresponding to an eddy viscosity of approximately 938 m^2 s^{-1}—a physically reasonable value for regions of high convective activity.

This regime is considered since it corresponds to a much more physically realistic situation where Newtonian damping is concentrated near the boundary layer and decays rapidly through the midtroposphere. When compared with the HND limit, it is intended to highlight the effects of boundary layer diffusion on the system in tandem with nonlinear effects.

(iii) The weak Newtonian damping and EBLD regime

The final regime we consider involves a much smaller value of $d_0 = 0.2$ in Eq. (20), corresponding to the physical situation in which nonlinear effects dominate in Eqs. (29) and (30). Here, we retain both the functional form of Newtonian damping which decays with height, setting $\gamma = 1/2$ in Eq. (20), and eddy viscosity with Re = 200. In order that the solutions remain regular in the weak damping regime, the same value of dimensional eddy viscosity as in the previous regime is used. Therefore, although the effect of diffusion as a whole is much less, the portion of it comprised of diffusion via eddy viscosity is greater.

Figures 4–6 below illustrate the velocity fields associated with the solutions to Eqs. (29) and (30). Although Eqs. (29) and (30) are posed in terms of the vertical component of the induced vorticity and the induced streamfunction, these quantities alone do not provide sufficiently intuitive explanations of the induced flow structure, and so we opt to present solutions in terms of the TCT and NCT induced velocity fields:

$$U(r, \theta, z) = \frac{\cos\theta \cos\lambda}{r} \Psi^N(r, z), \tag{40}$$

$$V(r, \theta, z) = -\sin\lambda \partial_r \Psi^T(r, z) - \sin\theta \cos\lambda \partial_r \Psi^N(r, z). \tag{41}$$

Brought to you by UNIVERSITY OF CALIFORNIA Davis - SERIALS RECORDS SECTION | Unauthenticated | Downloaded 07/14/25 03:45 PM UTC

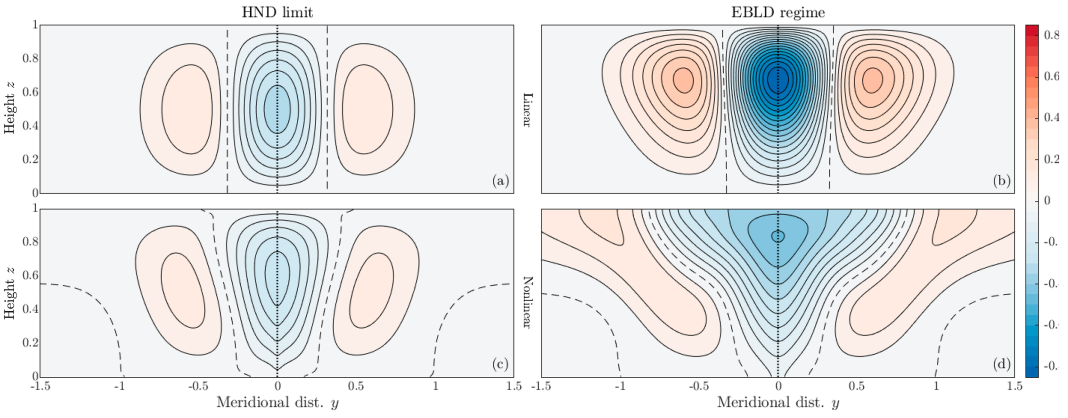

FIG. 5. Contour plots of the NCT induced zonal velocity $U^{x,N}$ as a function of (y, z). (a),(b) Linear solutions in the HND (with $d_0 = 1.5$) limit and EBLD (with $d_0 = 1.5$, Re = 200) regime, respectively, and (c),(d) the equivalent nonlinear solutions. Contours are shown at intervals of 0.05. Dashed lines correspond to zero contours, and the dotted line in each panel shows the equator ($\lambda = 0°$).

Since the flow induced by the TCT is axisymmetric, it is sufficient to represent the flow using the TCT induced component of azimuthal velocity $V^T(r, z)$. In contrast, the NCT induced flow is not axisymmetric, and so in order to represent the velocity field here, we project it onto the Cartesian $\hat{\mathbf{x}}$ basis vector and examine the zonal component of the NCT induced velocity field, given by

$$U^{x,N}(r, \theta, z) = \cos\lambda\left[\frac{\cos^2\theta}{r}\Psi^N(r, z) + \sin^2\theta\partial_r\Psi^N(r, z)\right]. \quad (42)$$

In each case shown, we use the heat source $S(r, z) = s(r)\sin(\pi z)$, and the artificial outer boundary is set at a value of $r_{\text{out}} = 5$.

Figure 4 shows the TCT induced azimuthal velocity $V^T(r, z) = -\partial_r\Psi^T(r, z)$ in regimes I and II in both the linear and nonlinear cases. The effect of the TCT is to induce an anticyclonic flow around the convective circulation in the upper troposphere and a cyclonic flow in the lower troposphere. It is immediately seen from Fig. 4a that in the linear case with the HND limit, this "twisting" motion is antisymmetric about the midtroposphere, leading to the presence of a shear plane at $z = 0.5$. It is apparent from Fig. 4c that the role of nonlinearity is significant in how the TCT affects the flow. The vorticity is advected by the poloidal flow so that the region of positive vorticity in the lower troposphere is advected radially inward and vertically upward, intensifying as kinetic energy is increased to conserve angular momentum (see e.g., Schubert and Alworth 1987, for an analogous discussion related to tropical cyclone development). Correspondingly, the negative vorticity decreases in intensity and is advected out and over the positive region. Consequently, the cyclonic portion of the flow is more intense and extends nearly the entire height of the troposphere with the shear layer being tilted almost up to the tropopause. It further becomes apparent as to the reason why eddy viscosity is necessary in order to maintain such a circulation. Recalling that the calculations in (Fig. 4c) are performed using an excessively small value for eddy viscosity ($\approx$47 m^2 s^{-1}), we see that the advection of the induced vorticity inward in the lower troposphere leads to a situation in which the gradient in azimuthal velocity becomes extreme and physically unrealistic at $r = 0$. Thus, an interior layer forms around the convective core which, from a physical standpoint, is untenable in the absence of further diffusive effects.

Figures 4b and 4d show that in the EBLD regime, the decreasing strength of the Newtonian damping with height leads to a situation in which the region of negative vorticity in the

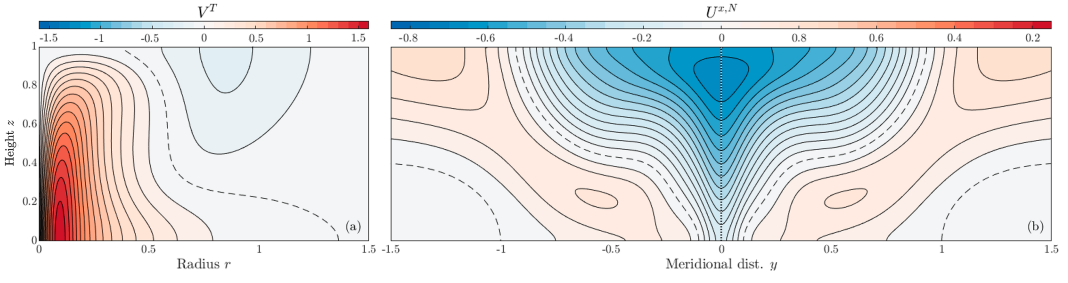

FIG. 6. Contour plots of the (a) nonlinear TCT induced azimuthal velocity V^T and (b) nonlinear NCT induced zonal velocity $U^{x,N}$ in the EBLD (with $d_0 = 0.2$, Re = 200) regime. Contour intervals are at 0.1 for (a) and 0.05 for (b). Dashed lines correspond to zero contours, and the dotted line in (b) shows the equator ($\lambda = 0°$).

Brought to you by UNIVERSITY OF CALIFORNIA Davis - SERIALS RECORDS SECTION | Unauthenticated | Downloaded 07/14/25 03:45 PM UTC

upper troposphere near the convective core is much greater than in the HND counterparts. Naturally, Fig. 4b shows that the antisymmetry about the midtroposphere is already broken in the linear case, with the upper region of anticyclonic flow being much greater in magnitude than the lower region of cyclonic flow. Furthermore, Fig. 4d shows that in the nonlinear regime, the upper layer of anticyclonic flow is approximately equal in magnitude to the lower region of cyclonic flow, suggesting that the nonlinearity has a damping effect on the induced flow. Once again, the poloidal flow advects the positive vorticity inward and the negative vorticity outward so that we have mostly cyclonic motion around the convective core and anticyclonic motion in the downwelling region outside.

Figure 5 shows meridional slices of the NCT induced zonal velocity in regimes I and II in both the linear and nonlinear cases. The zonal velocity slices are taken through the center of the circulation, so that in the Northern Hemisphere $\theta = \pi/2$ and in the Southern Hemisphere $\theta = -\pi/2$. Consequently, we represent $U^{x,N}$ and view Fig. 5 as though we were standing on the equator (shown with dotted lines) facing westward, so that positive/negative values of $U^{x,N}$ represent eastward/westward flow, respectively.

Figure 5a shows that in the linear case, the zonal velocity field is symmetric about the midtroposphere, with a region of westward flow along the equator with eastward flow to the north and south. The zero contours do not correspond to shear planes but rather lines about which the flow rotates (i.e., the stagnation points of a dipolar flow). If we were to introduce temporal perturbations to the system, these stagnation points would be much less dynamically significant than the shear plane in the analogous TCT case, and hence their advection by the poloidal flow (shown in Figs. 5c and 5d where nonlinear effects are present) is far less consequential for the stability of the flow. Thus, realistic solutions are possible in the absence of eddy viscosity when the damping is large, as shown in Fig. 5c.

In Figs. 5b and 5d for the EBLD regime, as for the TCT induced flow, the effect of the decreasing Newtonian damping with height is to increase the magnitude of vorticity in the upper troposphere. Thus, as nonlinear effects are included and the poloidal flow advects the induced vorticity upward and outward, the region of westward flow along the equator is lifted vertically, and extends laterally outward, away from the convective core. The region of eastward zonal flow is similarly lifted upward and extended outward, decreasing in magnitude so as to conserve angular momentum in the dipole. Thus, in effect, the nonlinearity in the vorticity equation acts to damp the NCT induced flow, decreasing the magnitude of the velocity field while extending it laterally outward in the upper troposphere.

Figure 6 shows the nonlinear solutions for both the TCT induced azimuthal velocity and the NCT induced zonal velocity for regime III above (i.e., the EBLD regime with $d_0 = 0.2$). In this regime, nonlinearity is dominant. Figure 6a shows that the region of positive TCT induced vorticity is drawn into the convective core so that the cyclonic portion of the flow intensifies and extends across the full height of the troposphere. In Fig. 6b, the NCT induced flow is less dramatically affected. The lifting effect of both the eastward and westward portions of the zonal flow is further exaggerated, and the lateral extent of the flow in the meridional direction is greater. Furthermore, the regions of eastward and westward zonal velocity appear to remain well separated, even when nonlinear effects are strong, and consequently, the overall structure of the flow appears to be robust.

c. *The induced streamfunction* $\Psi(r, \theta, z)$

Here, focusing primarily on the EBLD regime with both strong ($d_0 = 1.5$) and weak ($d_0 = 0.2$) Newtonian damping, we reconstruct the full three-dimensional induced streamfunction $\Psi(r, \theta, z)$ from Eq. (28) and discuss its implications for the convective circulation. Although the flow induced by rotation has a fully three-dimensional spatial dependence, its streamfunction representation arises from the fact that it lies firmly within the horizontal plane (i.e., there is no induced vertical component of velocity). With the understanding that fluid particles may only move vertically as a direct result of the diabatic heating which is encapsulated entirely by the poloidal component of the circulation, the most natural way to view the induced flow is through horizontal slices at fixed values of z.

Figure 7 shows contours of $\Psi(r, \theta, z)$ in horizontal slice planes over the height of the troposphere and at latitudes ranging from $\lambda = 0°$ (the equator, where only the NCT is present) to $\lambda = 90°$ (the North Pole, where only the TCT is present). At the North Pole, as expected, we see that the induced flow is rotationally symmetric, with anticyclonic rotation near the top of the troposphere and cyclonic rotation near the bottom. Here, the nonlinear interactions between the poloidal flow and the induced flow have the effect of pushing the region of cyclonic rotation up through the convective core, as is seen in Fig. 4, so that there is a small region of intense cyclonic rotation around the center of the circulation.

Arguably, the most striking feature of the induced flow is the east-to-west dipole structure seen at the lower latitudes caused by the NCT. At the equator, we see that an east-to-west wind is induced along the centerline of a convective circulation. We see that in the nonlinear regime, the east-to-west induced wind is maximized somewhere in the upper troposphere close to the tropopause. This is in contrast to the linear regime in the HND limit, where the strongest east-to-west induced wind occurs at the midtroposphere with no motion at all near the ground and the tropopause. Essentially, in the nonlinear EBLD regime, the upward advection of the east-to-west region of induced zonal flow breaks this symmetry, and since the boundary condition at the tropopause is free slip, fluid motion is permitted there. This dipole is seen to be somewhat stronger for weak Newtonian damping (when $d_0 = 0.2$), as can be seen in Figs. 8 and 9.

Figure 8 shows a detailed view of some of the more notable horizontal slice planes in the strong ($d_0 = 1.5$) and weak ($d_0 = 0.2$) Newtonian damping regimes. In all cases, the slice is taken at a value of $z = 0.85$ since this is the approximate height at which the maximum east-to-west induced velocity occurs at the equator (see Fig. 9). For both the $d_0 = 1.5$ and

Brought to you by UNIVERSITY OF CALIFORNIA Davis - SERIALS RECORDS SECTION | Unauthenticated | Downloaded 07/14/25 03:45 PM UTC

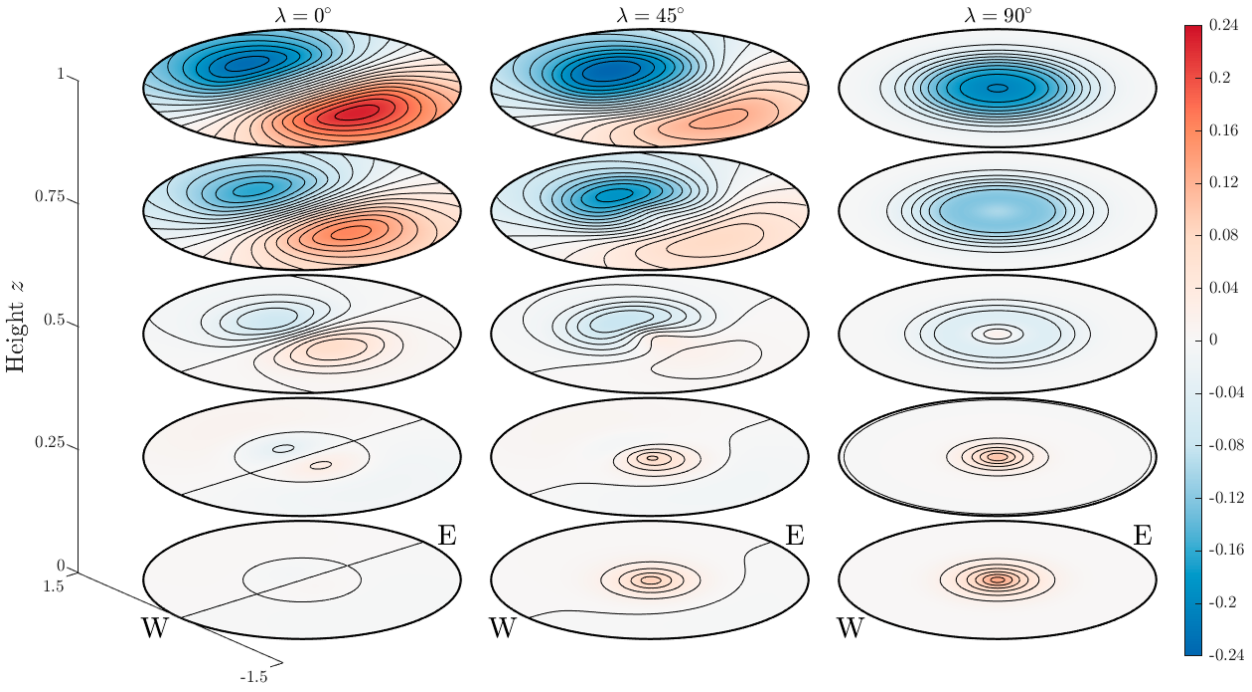

FIG. 7. Contour slices of the induced streamfunction $\Psi(r, \theta, z)$ at height intervals $z = 0, 0.25, 0.5, 0.75$, and 1 and latitudes $\lambda = 0°, 45°, 90°$ (shown from left to right). In all cases, the EBLD regime is adopted with Re = 200 and $d_0 = 1.5$. Contours are shown at intervals of 0.02.

$d_0 = 0.2$ cases, we see a strong east-to-west flow across the centerline of the circulation at the equator, with weaker anticyclonic circulations to the north and south. The minimum zonal velocity at the equator (i.e., the maximum east-to-west velocity) over the horizontal plane, which we denote as $U^x_{\min}(z)$, is seen to occur at the center of the circulation ($r = 0$). At the North Pole, we see cyclonic rotation when $d_0 = 1.5$; however, when $d_0 = 0.2$, we see cyclonic rotation immediately around the convective core with anticyclonic rotation further away. This is due to the stronger nonlinear effects which are present in the weak damping regime, which have the effect of drawing the positive portion of the TCT induced vorticity up through the convective core (see Fig. 4).

Figure 9 shows $U^x_{\min}(z)$ as a function of height in all the regimes we have considered. We see that in all cases, the maximum east-to-west velocity is greater and at a lower height for linear solutions than for their nonlinear counterparts. However, the east-to-west motion is more uniformly spread out over the height of the tropopause in the nonlinear regimes and does not vanish at the troposphere boundaries. For nonlinear solutions in the EBLD regime, the maximum east-to-west velocity occurs at approximately $z = 0.85$, since nonlinearity has the effect of "lifting" the east-to-west region of the zonal flow vertically. We further see that in the weak Newtonian damping case ($d_0 = 0.2$), the east-to-west flow is stronger than in the strong damping regime ($d_0 = 1.5$) but exhibits a very similar vertical structure.

In the nonlinear cases, the maximum nondimensional east-to-west velocities are 0.25 in the HND limit (0.52 m s^{-1}), 0.45 in the EBLD regime with strong Newtonian damping (0.94 m s^{-1}), and 0.27 in the EBLD regime with weak Newtonian damping (1.4 m s^{-1}). The dimensional magnitudes of the maximum east-to-west velocities, which are shown in parentheses, are found after multiplication by H/TRo, where we take $H = 15$ km, $T = 1200$ s, and Ro = 6. Immediately, it is seen (as would be expected from our asymptotic approach to the problem) that the east-to-west induced flow produced by the NCT is considerably weaker than the leading order poloidal flow and on these scales constitutes a second-order effect on the convective circulation. Moreover, as we move to larger scales in the atmosphere where the aspect ratio is much greater, these effects would be even less pronounced. This, however, ignores one of the subtle aspects of the NCT induced flow—namely, that the force produced by the east-to-west dipole structure will be constructively additive across a multitude of circulations. That is to say, taking the spatial average over a large area containing multiple circulations (as is typical in a numerical model), one finds that the net force is proportional to the number of circulations present. Thus, on scales where much larger circulations exist in tandem with these aspect ratio ≈ 1 circulations, although individually each circulation contributes only a small westward forcing, the net force produced by a cluster of circulations may have a leading-order effect on the large-scale dynamics. This principle will be discussed in more depth in the following section and formalized in a subsequent paper.

d. *Particle trajectories through a convective circulation*

With the poloidal streamfunction $\psi(r, z)$ and induced streamfunction $\psi(r, \theta, z)$ (and consequentially the full three-dimensional velocity field associated with the convective circulation) now fully specified and well understood, we

Brought to you by UNIVERSITY OF CALIFORNIA Davis - SERIALS RECORDS SECTION | Unauthenticated | Downloaded 07/14/25 03:45 PM UTC

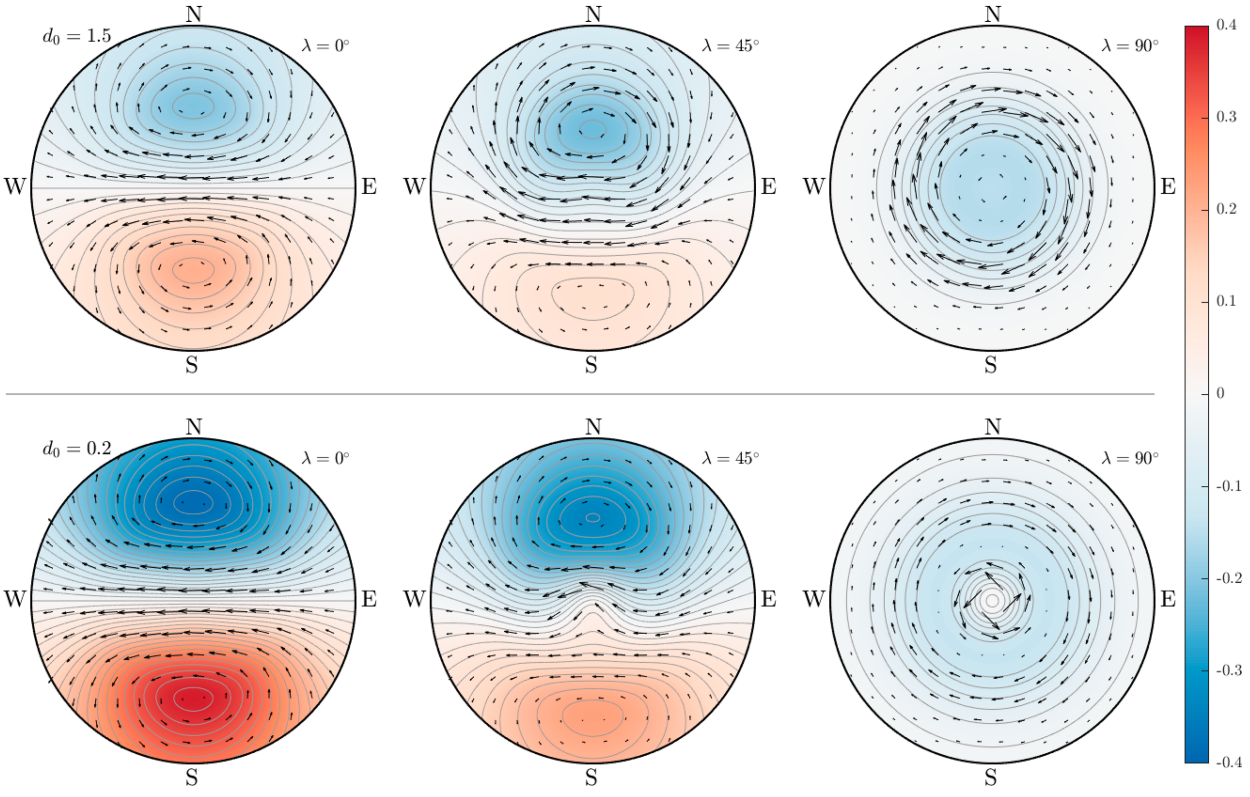

FIG. 8. Horizontal slices of the induced streamfunction Ψ at height $z = 0.85$. Latitudes $\lambda = 0°$, 45°, and 90° are shown for both (top) $d_0 = 1.5$ and (bottom) $d_0 = 0.2$. Contours are at intervals of 0.02, and vectors indicating the direction and magnitude of the flow are included in each case.

conclude this section by showing a selection of illustrative streamlines for the convective circulation. In terms of the PCV quantities $u(r, z)$ and $w(r, z)$ and the TCT/NCT components of the induced streamfunction $\Psi^T(r, z)$ and $\Psi^N(r, z)$, the velocity field, correct up to order $O(\mathrm{Ro}^{-2})$, is given in the cylindrical basis as

$$\mathbf{v}(r, \theta, z) = \left[u + \frac{\cos\lambda}{\mathrm{Ro}}\frac{\cos\theta}{r}\Psi^N\right]\hat{\mathbf{r}} - \frac{1}{\mathrm{Ro}}[\sin\lambda\partial_r\Psi^T + \sin\theta\cos\lambda\partial_r\Psi^N]\hat{\boldsymbol{\theta}} + w\hat{\mathbf{z}}. \quad (43)$$

The streamlines of our solution may be calculated from

$$\mathbf{x}_s(t) = \mathbf{x}_0 + \int_0^t \mathbf{v}[\mathbf{x}_s(\tau)]d\tau, \quad (44)$$

where $\mathbf{x}_s(t) = [r_s(t), \theta_s(t), z_s(t)]^{\mathrm{T}}$ denotes the position vector of a fluid parcel at time t and $\mathbf{x}_0 = \mathbf{x}(0)$ denotes its starting point. Calculating the streamlines directly from Eq. (44) is computationally expensive and is certainly nontrivial to do with numerical accuracy, and thus in practice, we exploit the stream3 command in MATLAB. Such a methodology has its drawbacks—namely, that since stream3 relies heavily on interpolation methods, it is not possible to integrate forward to a specific end time. Nonetheless, it suffices to provide a useful and aesthetically pleasing visual illustration of everything that we have discussed in this section. Figure 10 shows a selection of the most elucidating streamlines for the circulation. The streamline trajectories are started from seven groups of 12 points—one group arranged as 12 equally spaced points around a circle of radius 0.03 centered at the origin (red in Fig. 10), and the six other groups arranged in similar circles with their centers equally spaced around a circle of radius 0.2 centered at the origin. All trajectories are started at height $z = 0.1$.

Figures 10a and 10d, which consist only of the NCT component of the induced flow, show the westward pointing dipole induced by the NCT in action. That is, a particle which is initially located at the center of the circulation feels a westward force and consequently leaves the circulation to the west near the tropopause. Particles to the north and south of the equator experience a westward force during their ascent through the convective core and an eastward force during their descent further from the heat source. Notably, the effect of the NCT is subtle, but noticeable at these scales, with only a slight westward tilt to the convective structure visible. The convective circulation retains meridional symmetry about the line $y = 0$. Figures 10c and 10f show the convective circulation when only the TCT is present, and thus the circulation retains rotational symmetry. Importantly, as shown with the red trajectories, having ascended through the convective core, the fluid parcels are equally distributed around its circumference

Brought to you by UNIVERSITY OF CALIFORNIA Davis - SERIALS RECORDS SECTION | Unauthenticated | Downloaded 07/14/25 03:45 PM UTC

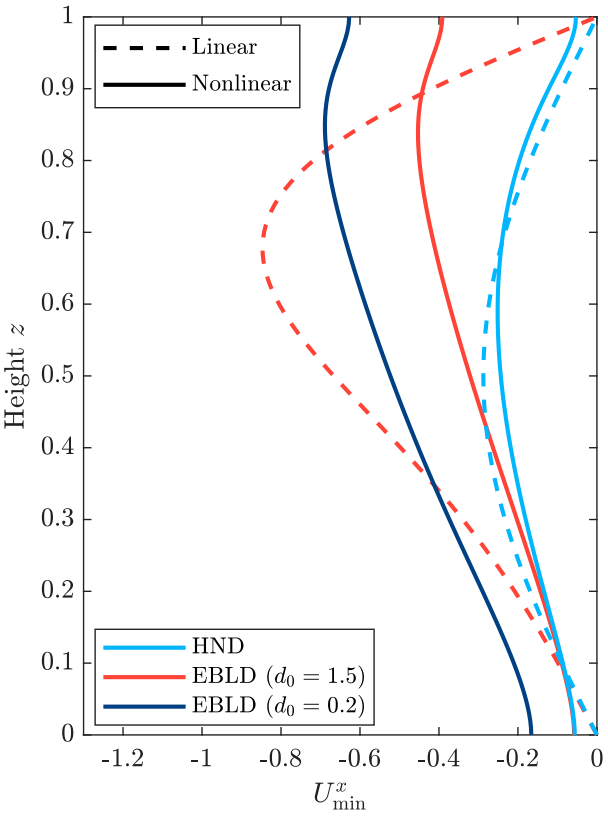

FIG. 9. Maximum east-to-west induced velocity $U^x_{\min}(z)$ plotted as a function of height in the HND limit and in the EBLD regime for both $d_0 = 1.5$ and $d_0 = 0.2$. Nonlinear results are shown using solid lines, and linear results are shown using dashed lines.

as they reach the tropopause and descend far from the heating region. Figures 10b and 10e contain contributions from both the TCT and NCT in equal measure and thus exhibit features of both the NCT induced flow (i.e., a westward bias to the fluid trajectories) and the TCT induced flow (i.e., an obvious anticyclonic rotation throughout the downwelling region). All symmetry is broken in this case.

4. Zonal forcing by subgrid-scale convection

In the previous sections, we detailed a new model for a nonlinear circulation driven by an axisymmetric heat source in the presence of both the TCT and NCT. The details of the circulation, while interesting from a physical and mathematical point of view, are of secondary importance in the context of weather and climate predictions, since in most instances the exact form of a convective circulation may not explicitly feature in large-scale models. In essence, the circulations are *subgrid scale*, i.e., the numerical grids used in GCMs and NWPs are too course to resolve the fluid dynamics associated with convection on the convective scale (Collins et al. 2013). Therefore, meteorologists will include convective processes via a subgrid-scale parameterization based upon the averaged dynamical quantities over a single grid box (Gregory 1997). In this section, we are concerned with determining the force exerted by a single convective circulation on its surroundings in the presence of the NCT, and consequently, the effect that subgrid-scale convection may have on the large-scale atmosphere, which is overlooked in models which neglect the NCT.

As a first step, let us define a grid box $\mathcal{G}$ as a square region in the x–y plane and define the average of a function $g(x, y, z)$ over such a grid box as

$$\langle g\rangle(z) = \frac{1}{|\mathcal{G}|}\iint_{\mathcal{G}} g(x, y, z)dxdy, \tag{45}$$

where $|\mathcal{G}|$ is the area of the grid box, and where we note that Eq. (45) assumes the grid box is centered at the origin. In our setup, where multiple noninteracting convective circulations exist within a grid box embedded inside a larger fluid, the gridbox boundary $\partial\mathcal{G}$, while nonphysical, in some sense, acts as an "insulator" between the subgrid-scale convection and the large-scale dynamics. That is, the effect of the convective circulation on the larger fluid may only be felt through its interaction with the gridbox boundary, and from the perspective of a large-scale observer, the grid box is a "black box."

It is well known (see e.g., Kershaw and Gregory 1997) that the primitive momentum equations for atmospheric dynamics on a resolved computational grid contain a forcing term (per unit mass) $\mathbf{F}(z)$ given by

$$\mathbf{F}(z) = -\frac{\partial}{\partial z}\langle \mathbf{v}w\rangle. \tag{46}$$

This function, which we term the *upscale flux convergence* function, describes the vertical gradient of the averaged momentum flux over the grid box and bears resemblance to the averaged flux convergence terms appearing in the large-scale equations in many multiple-scale analyses of convection in the atmosphere (see e.g., Majda and Klein 2003; Majda and Biello 2004; Boyd 2001; Biello and Majda 2005, 2010; Goldsmith and Esler 2023).

Let us consider the situation in which the grid box $\mathcal{G}$ contains n identical, well-separated convective circulations, so that individual convective circulations do not interact, and so that the ensemble average across the grid box may be assumed to coincide with a linear combination of the contributions from each individual convective circulation. We further define the constant a as the radius of the convective circulation updraft region, which for our purposes is chosen to coincide with the radial coordinate of the global maximum of the poloidal streamfunction $\psi(r, z)$. In this case, the averaging operator in Eq. (46) may be replaced by the operator $\langle\cdot\rangle_\infty$, which acts on a function $g(r, \theta, z)$ as

$$\langle g\rangle_\infty(z) = \frac{\mu}{\pi a^2}\int_0^{2\pi}\int_0^\infty g(r, \theta, z)rdrd\theta, \tag{47}$$

where $\mu = n\pi a^2/|\mathcal{G}|$ is the filling fraction (i.e., the fractional area of the grid box comprised of convective updraft regions). We note that in Eq. (47), the arbitrary function $g(r, \theta, z)$ represents a contribution to the ensemble of a single convective

Brought to you by UNIVERSITY OF CALIFORNIA Davis - SERIALS RECORDS SECTION | Unauthenticated | Downloaded 07/14/25 03:45 PM UTC

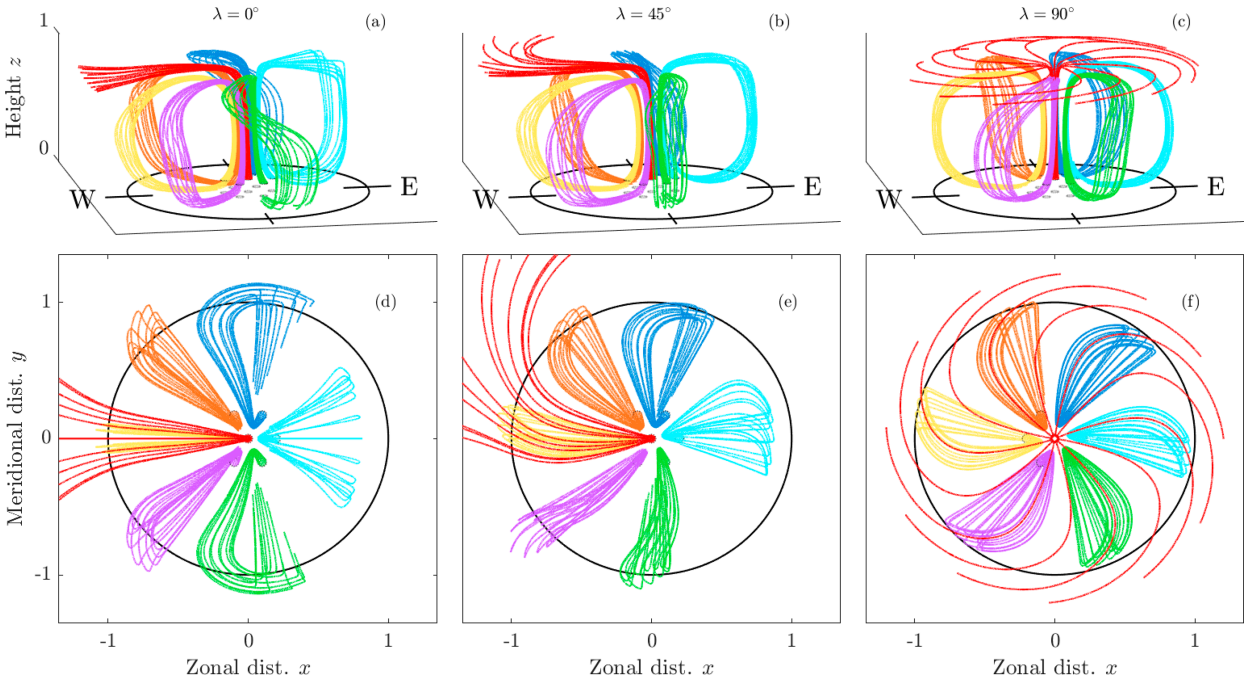

FIG. 10. A selection of streamlines for a circulation at latitudes $\lambda = 0°$, 45°, and 90° (shown from left to right). (a)–(c) A three-dimensional view of the circulation, and (d)–(f) a bird's eye view. In each case, the streamlines are started from seven groups of 12 points at a height 0.1 from the ground, the horizontal arrangement of which is described in the body of the text. Projections of the starting points onto $z = 0$ are shown as gray points in (a)–(c). In each case, the heat source is chosen as $S(r, z) = s(r)\sin(\pi z)$, and a value of $\mathrm{Ro} = 6$ is taken. In this figure, the convective circulation is in the nonlinear EBLD regime with $d_0 = 1.5$, $\mathrm{Re} = 200$.

circulation centered at the origin in polar coordinates, with the implicit assumption that it must decay over spatial scales smaller than the grid box. In accordance with the poloidal circulation depicted in Fig. 2, we choose $a = 0.42$.

Recalling that the full three-dimensional velocity field correct up to order $O(\mathrm{Ro}^{-2})$ is given by Eq. (43), we find

$$\mathbf{F}(z) = \mu\cos\lambda\hat{\mathbf{x}}\underbrace{\left[-\frac{1}{a^2\mathrm{Ro}}\frac{\partial}{\partial z}\int_0^\infty w\partial_r(r\Psi^N)dr\right]}_{F_1(z)} + \mu\hat{\mathbf{z}}\underbrace{\left[-\frac{2}{a^2}\frac{\partial}{\partial z}\int_0^\infty rw^2dr\right]}_{F_3(z)}. \tag{48}$$

The upscale flux convergence function in Eq. (48) has dimensions of acceleration, and thus its dimensional counterpart is recovered by multiplication with $W_{\max}^2/H \approx 0.01\,\mathrm{m\,s^{-2}}$ (or equivalently $\approx$900 m s^{-1} day^{-1}. The meridional component of the upscale flux convergence function $F_2(z)$ vanishes identically.

The vertical component of the upscale flux convergence function $F_3(z)$ is the simplest to understand, since it persists over all latitudes and has no dependence on the particular regime (i.e., linear/nonlinear or the particular form of diffusion). Indeed, since it depends only on the poloidal component of the vertical velocity, which in turn depends only on the form of the heating (due to the WTG), $F_3(z)$ is simply given in terms of the heating $S(r, z)$. Furthermore, when $w = s(r)\sin(\pi z)$, as in all calculations up until this point, then the vertical component of the upscale flux convergence function may be calculated analytically as

$$F_3(z) = -\frac{\pi}{20a^2}\sin(2\pi z). \tag{49}$$

Figure 11 shows a plot of $F_3(z)$ as a function of height z. There are no unexpectedly notable features of $F_3(z)$; however, it is worth taking a moment to view it in the context of a mean flow. Suppose that the mean perturbation pressure field and buoyancy of a large-scale atmospheric flow (denoted by $\overline{p}$ and $\overline{b}$, respectively,) are in hydrostatic balance in the absence of subgrid-scale convection. Thus, in the presence of convection, the vertical component of the momentum equation reads

$$\frac{\partial\overline{p}}{\partial z} = \overline{b} + \mu F_3(z). \tag{50}$$

There are two natural ways to interpret Eq. (50). First, one may "absorb" the forcing term into the buoyancy, so that the effect of convection is to decrease/increase the buoyant force in the lower/upper troposphere. Alternatively, the vertical integral of the forcing may be absorbed into the pressure, so that the "effective" mean pressure is given by

$$\overline{p}_{\mathrm{eff}} = \overline{p} - \mu\int_0^z F_3(z')dz'. \tag{51}$$

In either case, the effect is the same, and the vertical momentum equation [Eq. (50)] describes a *quasi*-hydrostatic balance between

Brought to you by UNIVERSITY OF CALIFORNIA Davis - SERIALS RECORDS SECTION | Unauthenticated | Downloaded 07/14/25 03:45 PM UTC

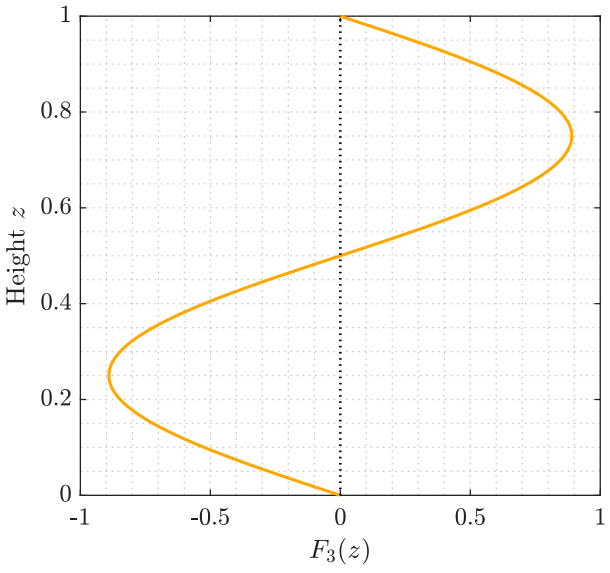

FIG. 11. The vertical component of the upscale flux convergence function $F_3(z) = -[\pi/(20a^2)]\sin(2\pi z)$. We choose $a = 0.42$.

an effective pressure and buoyancy (see e.g., White and Bromley 1995; Ong and Roundy 2020).

The zonal component of the upscale flux convergence function $F_1(z)$, which arises as a direct result of the NCT, is somewhat more complicated to understand but has a significantly more consequential effect on the the large-scale atmosphere than the vertical component. Figure 12 shows plots of $F_1(z)$ as a function of height z across multiple regimes of interest. In all cases, it is seen that the effect of convection—in particular, the component of the flow induced by the NCT—is to force a vertical shear at the large scale, with a westward force in the upper troposphere and an eastward force in the lower troposphere. We are able to conceptualize this result by understanding that the zonal component of the upscale flux convergence function $F_1(z)$ describes the average vertical gradient of the NCT induced momentum flux through horizontal planes over the grid box. Throughout most of the domain of the convective and NCT induced circulation, the flow is either upward/westward or downward/eastward, resulting in a vertical/westward-tilted convective structure. The domain average of the flux created by this circulation results in an upward transport of westward momentum and a compensating downward transport of eastward momentum. The convergence of this momentum flux yields a net force which is eastward in the lower troposphere and westward in the upper troposphere.

The presence of the zonal component of the upscale flux convergence function $F_1(z)$ provides a key insight into the effect of the NCT on atmospheric dynamics. That is, the NCT may be a fundamental mechanism contributing to the westward "vertical tilt" exhibited by convective structures in the tropics. Indeed, it is well known in particular that the *Madden–Julian oscillation* (MJO) propagates eastward with a zonal–vertical structure which tilts toward the west near the tropopause (Kiladis et al. 1994, 2005; Seiki and Takayabu 2007b; Lappen and Schumacher 2014; Hu and Li 2021). Furthermore, Majda and Biello (2004) and Biello and Majda (2005, 2010) showed that the westward-tilted structure of subgrid-scale convection was enough to recreate the westward vertical tilt in the MJO, though at the time a cause of the subgrid-scale westerly tilt had not been attributed to any dynamical principles compatible with their dynamical analysis and could only be added to their multiscale models artificially. Our results potentially provide the key ingredient missing from those previous studies.

Haertel and Kiladis (2004) and Kiladis et al. (2005) have suggested that the westward-tilted structure of the MJO is associated with convectively coupled waves and successfully reproduced many of the observed convective structures using a linear theory forced by a carefully calibrated diabatic heating source. This does not argue in opposition to the theory presented here, and it is likely that the two mechanisms each play a role. The key difference in our theory is that westward tilts are seen even in a stationary environment and arise as a result of a fundamental external force. Thus, it is arguable that westward tilts may be a much more ingrained feature of tropical

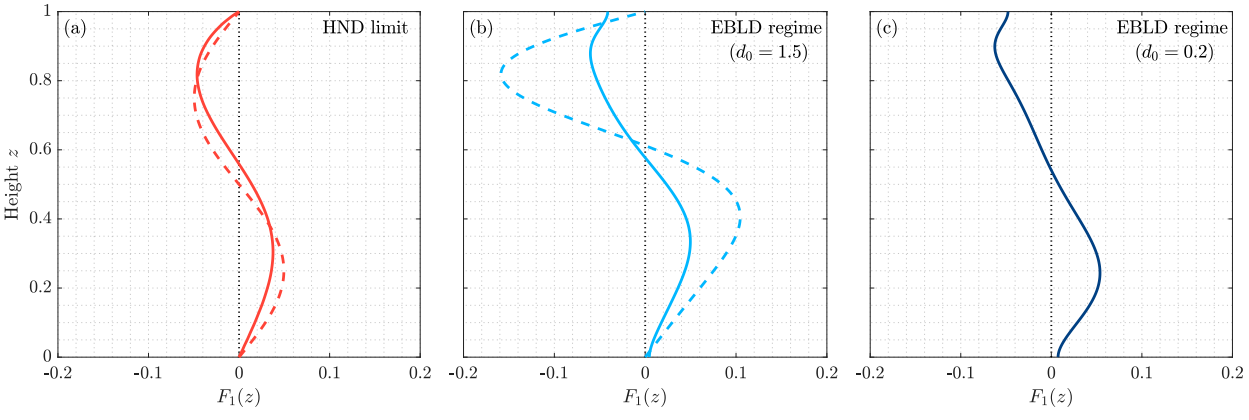

FIG. 12. The zonal component of the upscale flux convergence function $F_1(z)$ in the (a) HND limit and the EBLD regime for (b) $d_0 = 1.5$ and (c) $d_0 = 0.2$. Solid lines correspond to the nonlinear regime, and dashed lines correspond to the linear counterparts. In all cases, $a = 0.42$ is chosen.

Brought to you by UNIVERSITY OF CALIFORNIA Davis - SERIALS RECORDS SECTION | Unauthenticated | Downloaded 07/14/25 03:45 PM UTC

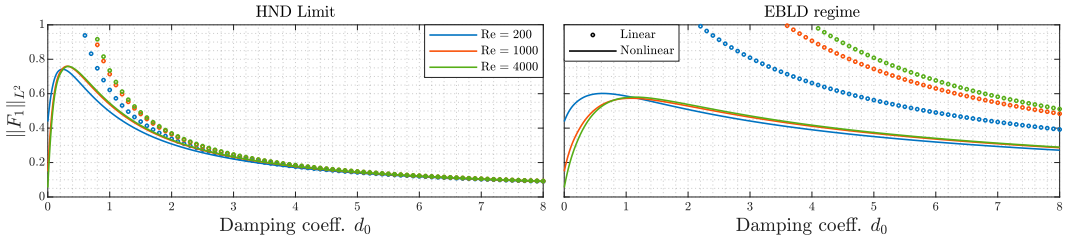

FIG. 13. The magnitude of the zonal upscale flux convergence function $\|F_1\|_{L^2}$ as a function of the damping coefficient d_0 in the (left) HND limit and (right) EBLD regime. Nonlinear results are shown with solid lines, and linear results are shown with circles. In each panel, the calculations are performed for Re = 200, 1000, 4000, shown in blue, red, and green, respectively. The heat source $S(r, z) = s(r)\sin(\pi z)$, and a value of $a = 0.42$ is used in each calculation.

convection than previously thought, arising at least in part from a frequently disregarded component of the Coriolis force.

Linear/nonlinear comparison

In the linear HND regime, Biello et al. (2024, manuscript submitted to *Quart. J. Roy. Meteor. Soc.*) find analytical expressions for the upscale flux convergence terms in the special case that the poloidal vertical velocity has a top-hat profile. In our case (omitting eddy viscosity), the linear version of Eq. (30) is given by

$$d(z)\left[\frac{1}{r}\partial_r(r\partial_r\Psi) - \frac{\Psi}{r^2}\right] = -w_r, \tag{52}$$

which is straightforwardly integrated to give

$$\partial_r(r\Psi) = -\frac{rw}{d(z)} + rC(z), \tag{53}$$

where $C(z)$ is an arbitrary function of z alone. Consequently, the zonal component of the upscale flux convergence function is found as

$$F_1(z) = \frac{1}{a^2\mathrm{Ro}}\frac{\partial}{\partial z}\left[\frac{1}{d(z)}\int_0^\infty rw^2 dr\right]. \tag{54}$$

Biello et al.'s (2024, manuscript submitted to *Quart. J. Roy. Meteor. Soc.*) result is explicitly recovered by replacing w with a top-hat profile across the updraft region and setting d constant in Eq. (54).

In the linear regime, $F_1(z) \propto 1/d_0$, and thus its magnitude decays monotonically as a function of d_0, while exhibiting singular behavior as $d_0 \to 0$. Importantly, in the weak damping limit, the linear regime must not be a valid approximation since this is when nonlinear effects are presumed to dominate. Figure 13 shows the magnitude (calculated from the L^2 norm $\|\cdot\|_{L^2}$) of the upscale flux convergence function $F_1(z)$ as a function of the damping coefficient d_0 in both the linear and nonlinear cases. It is seen that for large d_0, the nonlinear results asymptotically approach their linear counterparts. The coincidence of the results as $d_0 \to \infty$ is particularly obvious in the HND limit where damping has an equally strong effect throughout the troposphere, though convergence is also observed in the EBLD regime. Perhaps more notably, as $d_0 \to 0$, we see that the nonlinear results do not exhibit singular behavior and remain bounded. Our results indicate that the magnitude of the upscale flux convergence achieves a maximum for some small value of d_0, before rapidly decreasing as $d_0 \to 0$. The exact asymptotic form of the upscale flux convergence in the weak damping limit is yet to be established and will be the topic of a future study.

5. Conclusions

In this study, we derived an asymptotic system of equations describing a steady convective circulation driven by an axisymmetric heat source in the presence of the full Coriolis force. Our work provides an important generalization of the linear circulation solutions derived by Marsico et al. (2023, 2024) and the upscale flux convergence results of Biello et al. (2024, manuscript submitted to *Quart. J. Roy. Meteor. Soc.*) into the nonlinear regime. Those authors previously showed that in the linear regime the circulation may be decomposed into two main components—namely, the poloidal circulation and the secondary flow induced by rotation. Furthermore, the secondary flow may be decomposed into lower-level cyclonic and upper-level anticyclonic rotation induced by the TCT and a midlevel, westward-pointing dipole induced by the NCT which forces a westward tilt in convection. The results presented here provide concrete evidence that the same basic flow structure persists across regimes which involve nonlinear effects. It is further shown that westward-tilted convection is still a notable feature and drives similar vertical shear structures at larger scales but that the linear results provide only a rough approximation in some limited regimes of interest. Here, the regimes of validity have been vastly extended.

Ultimately, we expect that our results provide a necessary next step in the accurate parameterization of convection, by accounting for an additional contribution to the vertical shear that westward-tilted subgrid-scale convection imparts upon the large-scale atmosphere. To properly achieve this goal, however, there are a number of additional steps that must be taken. The first and most obvious step is to recognize that we have sacrificed the neat analytical expression of the upscale flux convergence parameterization that the linear case provides, in favor of a more general and accurate nonlinear

Brought to you by UNIVERSITY OF CALIFORNIA Davis - SERIALS RECORDS SECTION | Unauthenticated | Downloaded 07/14/25 03:45 PM UTC

counterpart which thus far has not been expressed analytically in terms of easily diagnosed parameters. That is not to say that accurate analytical representations of the nonlinear fluxes are not achievable; however, it is apparent that doing so will require additional work, and thus their determination will be left as a topic for future studies.

Another shortcoming of the present work is the fact that we began with a steady-state model, maintained by a prescribed diabatic heat source. In future work, it would be more enlightening to include a dynamically active moisture field in the system while allowing for temporal variations in the circulation—in particular, the vertical shear of zonal velocity. It is well known that moist processes are of vital importance in driving atmospheric dynamics (Klein and Majda 2006; Hittmeir and Klein 2018), particularly when dealing with tropical convection. It seems, therefore, that understanding the effects of such a moisture field on the upscale momentum fluxes provided by the NCT is of great significance. Fortunately, the prospects for such a study seem positive since we have already shown that the flow structures induced by rotation are robust and exhibit the same basic features across numerous dry regimes. Moreover, the DoNUT framework of Igel and Biello (2020) which has subsequently proved its utility in numerous studies (this one included) provides the ideal base model around which to build a dynamical moisture field and to investigate its effects.

Finally, it remains an important step in the greater context of this work to test the validity of our upscale flux convergence parameterization by examining the effects of subgrid-scale convection in the presence of the NCT on large-scale tropical systems. Such tests may be conducted in a variety of manners, either by directly including our parameterizations in numerical weather simulations or by developing multiple-scale asymptotic theories. Previous multiple-scale theories such as those of Majda and Klein (2003), Majda and Biello (2004), and Biello and Majda (2005, 2010, 2013) lend themselves well to such investigations, with the MJO theories in particular having already discussed the likelihood of subgrid-scale tilting being of importance. Notably, the DoNUT once again provides the perfect framework around which to build these models, with similar circulations having been a key component in the multiple-scale wave theory of Goldsmith and Esler (2023).

To summarize, the nonlinear work here generalizes the linear results for TCT and NCT induced convective circulations and brings us one important step closer to being able to parameterize their effects in numerical models. Going forward, we recognize the importance of relaxing a number of idealized assumptions as well as providing rigorous testing of our upscale flux theories in a multiple-scale settings.

Acknowledgments. This work was partially supported by the NSF under Award AGS-2224293 and by the Krener Assistant Professorship at UC Davis.

Data availability statement. No datasets were generated or analyzed during the current study.

REFERENCES

Biello, J. A., and A. J. Majda, 2005: A new multiscale model for the Madden–Julian oscillation. *J. Atmos. Sci.*, **62**, 1694–1721, https://doi.org/10.1175/JAS3455.1.

——, and ——, 2010: Intraseasonal multi-scale moist dynamics of the tropical atmosphere. *Commun. Math. Sci.*, **8**, 519–540, https://doi.org/10.4310/CMS.2010.v8.n2.a11.

——, and ——, 2013: A multiscale model for the modulation and rectification of the ITCZ. *J. Atmos. Sci.*, **70**, 1053–1070, https://doi.org/10.1175/JAS-D-12-0142.1.

Boyd, J. P., 2001: *Chebyshev and Fourier Spectral Methods*. Dover Publications, 668 pp.

Charney, J. G., and A. Eliassen, 1964: On the growth of the hurricane depression. *J. Atmos. Sci.*, **21**, 68–75, https://doi.org/10.1175/1520-0469(1964)021%3C0068:OTGOTH%3E2.0.CO;2.

Collins, S. N., R. S. James, P. Ray, K. Chen, A. Lassman, and J. Brownlee, 2013: Grids in numerical weather and climate models. *Climate Change and Regional/Local Responses*, Y. Zhang and P. Ray, Eds., IntechOpen, 111–128, https://doi.org/10.5772/55922.

Coriolis, G.-G., 1835: Memoire sur les equations du mouvement relatif des systemes de corps. *J. Ecol. Polytech.*, **24**, 142–154.

Deremble, B., 2016: Convective plumes in rotating systems. *J. Fluid Mech.*, **799**, 27–55, https://doi.org/10.1017/jfm.2016.348.

Emanuel, K. A., J. D. Neelin, and C. S. Bretherton, 1994: On large-scale circulations in convecting atmospheres. *Quart. J. Roy. Meteor. Soc.*, **120**, 1111–1143, https://doi.org/10.1002/qj.49712051902.

Goldsmith, E. J., and J. G. Esler, 2023: Wave propagation through a stationary field of clouds: A homogenisation approach. *Quart. J. Roy. Meteor. Soc.*, **149**, 3455–3476, https://doi.org/10.1002/qj.4567.

Gregory, D., 1997: The mass flux approach to the parametrization of deep convection. *The Physics and Parameterization of Moist Atmospheric Convection*, R. K. Smith, Ed., Springer, 297–319, https://doi.org/10.1007/978-94-015-8828-7_12.

Hack, J. J., and W. H. Schubert, 1986: Nonlinear response of atmospheric vortices to heating by organized cumulus convection. *J. Atmos. Sci.*, **43**, 1559–1573, https://doi.org/10.1175/1520-0469(1986)043<1559:NROAVT>2.0.CO;2.

Haertel, P. T., and G. N. Kiladis, 2004: Dynamics of 2-day equatorial waves. *J. Atmos. Sci.*, **61**, 2707–2721, https://doi.org/10.1175/JAS3352.1.

Held, I. M., and A. Y. Hou, 1980: Nonlinear axially symmetric circulations in a nearly inviscid atmosphere. *J. Atmos. Sci.*, **37**, 515–533, https://doi.org/10.1175/1520-0469(1980)037<0515:NASCIA>2.0.CO;2.

——, and B. J. Hoskins, 1985: Large-scale eddies and the general circulation of the troposphere. *Atmospheric and Oceanic Modeling*, B. Saltzman, Ed., Advances in Geophysics, Vol. 28, Elsevier, 3–31, https://doi.org/10.1016/S0065-2687(08)60218-6.

Helmholtz, H., 1867: LXIII. On integrals of the hydrodynamical equations, which express vortex-motion. *Lond. Edinb. Dubl. Philos. Mag. J. Sci.*, **33**, 485–512, https://doi.org/10.1080/14786446708639824.

Hittmeir, S., and R. Klein, 2018: Asymptotics for moist deep convection I: Refined scalings and self-sustaining updrafts. *Theor. Comput. Fluid Dyn.*, **32**, 137–164, https://doi.org/10.1007/s00162-017-0443-z.

Holton, J. R., 2004: *An Introduction to Dynamic Meteorology*. Vol. 88. Elsevier Science, 535 pp., https://books.google.com/books?id=fhW5oDv3EPsC.

Brought to you by UNIVERSITY OF CALIFORNIA Davis - SERIALS RECORDS SECTION | Unauthenticated | Downloaded 07/14/25 03:45 PM UTC

Hu, F., and T. Li, 2021: Effects of MJO vertically tilted structure on its phase speed from the moisture mode theory perspective. *J. Climate*, **34**, 4505–4520, https://doi.org/10.1175/JCLI-D-20-0732.1.

Igel, M. R., and J. A. Biello, 2020: The nontraditional Coriolis terms and tropical convective clouds. *J. Atmos. Sci.*, **77**, 3985–3998, https://doi.org/10.1175/JAS-D-20-0024.1.

Kershaw, R., and D. Gregory, 1997: Parametrization of momentum transport by convection. I: Theory and cloud modelling results. *Quart. J. Roy. Meteor. Soc.*, **123**, 1133–1151, https://doi.org/10.1002/qj.49712354102.

Kiladis, G. N., G. A. Meehl, and K. M. Weickmann, 1994: Large-scale circulation associated with westerly wind bursts and deep convection over the western equatorial Pacific. *J. Geophys. Res.*, **99**, 18 527–18 544, https://doi.org/10.1029/94JD01486.

——, K. H. Straub, and P. T. Haertel, 2005: Zonal and vertical structure of the Madden–Julian oscillation. *J. Atmos. Sci.*, **62**, 2790–2809, https://doi.org/10.1175/JAS3520.1.

Klein, R., 2010: Scale-dependent models for atmospheric flows. *Annu. Rev. Fluid Mech.*, **42**, 249–274, https://doi.org/10.1146/annurev-fluid-121108-145537.

——, and A. J. Majda, 2006: Systematic multiscale models for deep convection on mesoscales. *Theor. Comput. Fluid Dyn.*, **20**, 525–551, https://doi.org/10.1007/s00162-006-0027-9.

Lappen, C.-L., and C. Schumacher, 2014: The role of tilted heating in the evolution of the MJO. *J. Geophys. Res. Atmos.*, **119**, 2966–2989, https://doi.org/10.1002/2013JD020638.

Lebovitz, N. R., 1989: The stability equations for rotating, inviscid fluids: Galerkin methods and orthogonal bases. *Geophys. Astrophys. Fluid Dyn.*, **46**, 221–243, https://doi.org/10.1080/03091928908208913.

LeMone, M. A., 1983: Momentum transport by a line of cumulonimbus. *J. Atmos. Sci.*, **40**, 1815–1834, https://doi.org/10.1175/1520-0469(1983)040<1815:MTBALO>2.0.CO;2.

Liang, X., and J. C. L. Chan, 2005: The effects of the full Coriolis force on the structure and motion of a tropical cyclone. Part I: Effects due to vertical motion. *J. Atmos. Sci.*, **62**, 3825–3830, https://doi.org/10.1175/JAS3545.1.

Majda, A. J., and R. Klein, 2003: Systematic multiscale models for the tropics. *J. Atmos. Sci.*, **60**, 393–408, https://doi.org/10.1175/1520-0469(2003)060%3C0393:SMMFTT%3E2.0.CO;2.

——, and J. A. Biello, 2004: A multiscale model for tropical intraseasonal oscillations. *Proc. Natl. Acad. Sci. USA*, **101**, 4736–4741, https://doi.org/10.1073/pnas.0401034101.

Marsico, D. H., J. A. Biello, and M. R. Igel, 2023: Balanced convective circulations in a stratified atmosphere. Part I: A framework for assessing radiation, the Coriolis force, and drag. *J. Atmos. Sci.*, **80**, 2915–2924, https://doi.org/10.1175/JAS-D-22-0254.1.

——, ——, and ——, 2024: Balanced convective circulations in a stratified atmosphere. Part II: Circulations in the presence of radiation and the non-traditional Coriolis terms. *Geophys. Astrophys. Fluid Dyn.*, **118**, 1–24, https://doi.org/10.1080/03091929.2023.2292667.

Montgomery, M. T., and B. F. Farrell, 1993: Tropical cyclone formation. *J. Atmos. Sci.*, **50**, 285–310, https://doi.org/10.1175/1520-0469(1993)050<0285:TCF>2.0.CO;2.

——, H. D. Snell, and Z. Yang, 2001: Axisymmetric spindown dynamics of hurricane-like vortices. *J. Atmos. Sci.*, **58**, 421–435, https://doi.org/10.1175/1520-0469(2001)058<0421:ASDOHL>2.0.CO;2.

Ong, H., and P. E. Roundy, 2020: Nontraditional hypsometric equation. *Quart. J. Roy. Meteor. Soc.*, **146**, 700–706, https://doi.org/10.1002/qj.3703.

Pedlosky, J., 1987: *Geophysical Fluid Dynamics*. Springer-Verlag, 710 pp.

Poisson, S. D., 1838: Sur le mouvement des projectiles dans l'air, en ayant egard a la rotation de le terre. *J. Ecol. Polytech.*, **16**, 1–226.

Rotunno, R., and K. A. Emanuel, 1987: An air–sea interaction theory for tropical cyclones. Part II: Evolutionary study using a nonhydrostatic axisymmetric numerical model. *J. Atmos. Sci.*, **44**, 542–561, https://doi.org/10.1175/1520-0469(1987)044%3C0542:AAITFT%3E2.0.CO;2.

Schubert, W. H., and J. J. Hack, 1982: Inertial stability and tropical cyclone development. *J. Atmos. Sci.*, **39**, 1687–1697, https://doi.org/10.1175/1520-0469(1982)039%3C1687:ISATCD%3E2.0.CO;2.

——, and B. T. Alworth, 1987: Evolution of potential vorticity in tropical cyclones. *Quart. J. Roy. Meteor. Soc.*, **113**, 147–162, https://doi.org/10.1002/qj.49711347509.

Seiki, A., and Y. N. Takayabu, 2007a: Westerly wind bursts and their relationship with intraseasonal variations and ENSO. Part I: Statistics. *Mon. Wea. Rev.*, **135**, 3325–3345, https://doi.org/10.1175/MWR3477.1.

——, and ——, 2007b: Westerly wind bursts and their relationship with intraseasonal variations and ENSO. Part II: Energetics over the western and central Pacific. *Mon. Wea. Rev.*, **135**, 3346–3361, https://doi.org/10.1175/MWR3503.1.

Smith, R. K., 1980: Tropical cyclone eye dynamics. *J. Atmos. Sci.*, **37**, 1227–1232, https://doi.org/10.1175/1520-0469(1980)037<1227:TCED>2.0.CO;2.

——, and S. Vogl, 2008: A simple model of the hurricane boundary layer revisited. *Quart. J. Roy. Meteor. Soc.*, **134**, 337–351, https://doi.org/10.1002/qj.216.

——, and M. T. Montgomery, 2010: Hurricane boundary-layer theory. *Quart. J. Roy. Meteor. Soc.*, **136**, 1665–1670, https://doi.org/10.1002/qj.679.

——, and ——, 2016: The efficiency of diabatic heating and tropical cyclone intensification. *Quart. J. Roy. Meteor. Soc.*, **142**, 2081–2086, https://doi.org/10.1002/qj.2804.

——, ——, and G. L. Thomsen, 2014: Sensitivity of tropical-cyclone models to the surface drag coefficient in different boundary-layer schemes. *Quart. J. Roy. Meteor. Soc.*, **140**, 792–804, https://doi.org/10.1002/qj.2057.

Sobel, A. H., J. Nilsson, and L. M. Polvani, 2001: The weak temperature gradient approximation and balanced tropical moisture waves. *J. Atmos. Sci.*, **58**, 3650–3665, https://doi.org/10.1175/1520-0469(2001)058<3650:TWTGAA>2.0.CO;2.

Sutherland, B. R., and Coauthors, 2021: Plumes in rotating fluid and their transformation into tornados. *J. Fluid Mech.*, **924**, A15, https://doi.org/10.1017/jfm.2021.618.

Taylor, S. G., 1959: The present position in the theory of turbulent diffusion. *Advances in Geophysics*, Vol. 6, Elsevier, 101–112, https://doi.org/10.1016/S0065-2687(08)60097-7.

Trefethen, L. N., 2000: *Spectral Methods in MATLAB*. SIAM, 165 pp.

Vallis, G. K., 2017: *Atmospheric and Oceanic Fluid Dynamics: Fundamentals and Large-Scale Circulation*. 2nd ed. Cambridge University Press, 946 pp.

White, A. A., and R. A. Bromley, 1995: Dynamically consistent, quasi-hydrostatic equations for global models with a complete representation of the Coriolis force. *Quart. J. Roy. Meteor. Soc.*, **121**, 399–418, https://doi.org/10.1002/qj.49712152208.

Brought to you by UNIVERSITY OF CALIFORNIA Davis - SERIALS RECORDS SECTION | Unauthenticated | Downloaded 07/14/25 03:45 PM UTC